Modeling a gas sensor based on quantum vacuum fluctuations

Master thesis in Physics

Theoretical Atomic, Nuclear and Particle Physics

by

Eivind Kristen Osestad

Department of Physics and Technology

University of Bergen

June 01, 2022

Abstract

This thesis presents a model of a gas sensor that uses quantum vacuum fluctuations to find the concentration of CO_2 in a mixture of other gases, to demonstrate that such a sensor might be possible to make.

Our model is a hollow-core fiber of silicon dioxide with spheres of different dielectric materials suspended in an optical trapping potential generated by a standing laser field.

We show that there are dispersion forces between the fiber and the spheres due to virtual photons propagating from the sphere through the gas, scattering off the wall, and propagating back to the spheres. We show how this leads to the gas mixture screening the dispersion force by a different amount for the different spheres, leading to different changes in trapping frequency.

Finally, an artificial neural network is trained to find the relationship between the trapping frequencies and the partial pressure of CO_2 in the mixture. Thus, we show that the gas concentration can be measured using quantum vacuum fluctuation, and achieve a mean square error of 4.27×10^{-9} atm^2.

Acknowledgments

First of all, I would like to thank my family for their support, especially my sister who came to Bergen to study as well. I would also like to thank my friends, both my older ones and the members of my band, The Wanks, who have made my study breaks over the last year so much more fun and effective, which has been extremely helpful.

Most of all, I would like to thank my supervisor Johannes Fielder for being immeasurably helpful. He has always answered my questions or pointed me to a book or paper that has just the answers I need. His great trust in my abilities has also pushed me to do a better job than I could have otherwise done.

Contents

Chapter 1

Introduction

A recent challenge in chemical and bio-sensing is the detection of few or even single particles [1, 2, 3]. This has many possible applications, such as in medicine [4, 5, 6].

Light spectroscopy is a common method used to sense the concentration of different gases in a mixture. Spectroscopy looks at the response of the gas mixture to light, which is the same as saying how it reacts to photons. As different molecules absorb and emit light at different wavelengths it is possible to find what amount of different molecules are present in a gas mixture, and if you look at a large enough part of the spectrum you can distinguish multiple gases from one another.

In section 3.1 we explain how quantum vacuum fluctuations of the electromagnetic field act via virtual photons. These cannot be measured the way real photons can. However, they have indirect effects, such as creating dispersion forces between dielectric objects. Dispersion forces are forces such that arise as consequences of quantum ground state fluctuations [7, p.747]. Examples of such forces are Casimir forces between bodies [8], van der Waals forces between atoms [9, 10] and Casimir-Polder forces between atoms and bodies [10].

This thesis presents a model of a gas sensor, that is based on these fluctuations. It measures the screening effect of the gas on the quantum vacuum fluctuations indirectly, through its effect on a system of dielectric materials. Machine learning techniques will then be used to reverse the relationship between the screening effect of the gas mixture, and the concentrations of gases in the system. Essentially, we do a sort of indirect spectroscopy on the gas mixture using virtual photons. The hope is that this type of sensor can be developed to a point where it can detect small consentrations of a gas

We will first give an overview of the sensor we intend to model. Then a short introduction

to machine learning techniques. Followed by a section dedicated to explaining the theory of dielectric responses, quantum electrodynamics with and without the presence of dielectric materials, and an explanation of the Casimir–Polder interactions describing all the forces of the considered system. Then we discuss the machine learning part of the project before we conclude the thesis by introducing a CO_2-gas sensor. As this thesis main goal is to demonstrate the viability of a quantum vacuum fluctuation gas sensor the choice of gas is not very important. However, CO_2 is a very important greenhouse gas and its dispersion force related properties have several interesting properties [11, 12, 13]

1.1 Model Introduction

The gas sensor considered here is a hollow-core fiber, which is a small hollow cylinder, with a collection of dielectric spheres suspended in a standing laser field. The inner hollow part is set to a radius of 500 nm and the thickness of the wall is 500 nm, the total radius of the cylinder is 1000 nm. We consider the wall to be made out of silicon dioxide, which is experimentally acquirable, and its dielectric properties are known [14]. An illustration of part of the cross-section of the cylinder is shown in figure 1.1.

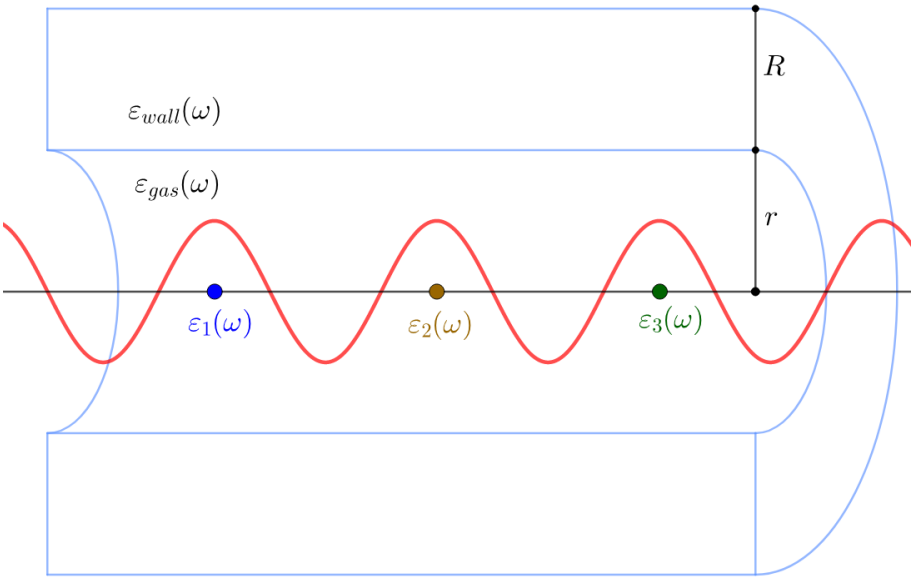

Figure 1.1: Illustration of a part of the cross section of our model with dielectric spheres ε_i and the standing laser field (red line) in a hollow-core fiber with inner radius r, and outer radius R, and dielectric function ε_{wall}. The gas with permittivity ε_{gas} flows within the fiber.

Inside the fiber, there is a standing laser field. Ten dielectric spheres with 10 nm radii

are suspended due to the optical trapping potential created by the electromagnetic field of the laser. This potential arises since the spheres are polarizable and therefore they will be pulled towards where the magnitude of the electric field is strongest. Each of the spheres is made of different dielectric materials. Due to the shape of the trapping potential, the spheres oscillate back and forth around the middle of the cylinder, and the peaks of the standing waves. Due to thermal fluctuations, they never stand still at the center of the potential.

In classical electromagnetism, the optical trapping potential would be the only source of forces on the spheres. However, taking into account quantum electrodynamics, one finds that there arise dispersion forces between the atoms in the sphere and the wall of the cylinder. The forces between dielectric bodies and polarizable atoms are known as the Casimir–Polder force[7, p.749]. We describe it in terms of the Casimir–Polder potential. We show later in this thesis that this force can be interpreted as arising from virtual photons propagating from the sphere through the gas scattering in the wall and then returning to the sphere. The effect on the sphere from the sum of all these virtual photons adds up to be the Casimir–Polder potential.

The idea behind this thesis is that these photons travel through the gas leading to a screening of the force [15]. For this reason, the trapping frequencies depend on the values and relationships between the dielectric functions of the spheres, the gas, and the wall. Thus, different gas mixtures will change the trapping frequency by different amounts. If we have multiple spheres all having their trapping frequency changed by different amounts by different gas mixtures, we might be able to reverse the problem and find the composition of the gas mixture only by knowing the trapping frequencies.

1.2 Machine Learning Introduction

We will show in later sections that the relationship between the dielectric functions of the wall, the gases, and the spheres is not a simple one. For this reason, finding the inverse relationship will be a very difficult task where we to try to do it analytically. Instead, we use machine learning techniques to find this relationship.

Machine learning programs repeatedly perform a task to gain experience with it. Every time it performs the task, the performance of the program is measured by some metric, known as a loss. The program then changes its approach to try to minimize or maximize the loss, by learning and generalizing the knowledge about the training system.[16]

In our case, the task is to find, as closely as possible, the partial pressure of CO_2 inside a mixture of nine other gases. By generating a large number of gas mixtures, we can train our machine learning program by giving it a mixture, having it guess the partial pressure, and then telling it how far off it was from the real value. By repeating this learning process a large number of times, the program should learn how to find the partial pressure of CO_2 from our list of trapping frequencies.

An artificial neural network will be used and trained on the relation between concentration and trapping frequency. Such a network works by taking in a vector, performing a series of linear transformations on it, and then putting out a new vector. In our case the input vector will be a list of the trapping frequencies and the output will be guesses for the partial pressure of CO_2 in the gas mixture corresponding to these trapping frequencies. The parameters of the matrices in the program are gradually changed after each guess to decrease the gap between the guess and the correct value.

1.3 Thesis Objectives

The overall aim of this thesis has been to create a first theoretical model of a new type of compound-specific gas sensor, which works by measuring the screening effect of the gas on the quantum vacuum fluctuations indirectly, through its effect on a system of dielectric materials. The idea of this new type of sensor stems from the main supervisor Dr. Johannes Fiedler. The objectives leading to the overall aim can be summarized as follows:

1. Setting up a theoretical model for the sensor response function.
2. Setting up a theoretical model for gas responses that can be used to train a machine learning program.
3. Train a machine learning program with the test cases developed in 2.
4. Test the sensor with new gas mixtures to obtain values for its measurement uncertainty.

Chapter 2

Theory

The following chapter introduces the theoretical background needed to calculate the dispersion forces relevant to our system as well as to calculate the trapping frequency due to the optical potential.

First, we consider linear response functions as a description of dielectric responses. Thereafter we go through the second quantization scheme for the free electromagnetic field, then redo the quantization with the coupling to dielectric media. Afterward, we describe the response of a neutral dielectric sphere to the electric field, thus, allowing us to derive the Casimir–Polder force which arises from quantum field interactions with neutral atoms.

2.1 Linear response functions

In this section, we describe linear response functions because several important properties of our model are described by such a function, such as the electric susceptibility, see section 2.3, and the polarizability of the spheres, see section 2.4. In addition, we describe some important properties that these functions have and introduce an important transformation known as the Kramers–Kronig relation.

A linear response function, $\alpha(t)$, is a function that gives the response of a system, $p(t)$, by applying an external field, $E(t)$, in terms of a convolution with the source

$$p(t) = \int_{-\infty}^{\infty} d\tau \alpha(\tau) E(t-\tau)\,. \tag{2.1.1}$$

As we are dealing with physical systems more assumptions can be made about these responses. All equilibrium physical response functions must obey causality, which means that

the response does not depend on previous states. This is achieved by having $\alpha(t) = \theta(t)Y(t)$, where $Y(t) = \alpha(t)$ for positive values of t, and arbitrary for negative values of t, and $\theta(t)$ is the Heaviside step function

$$\theta(t) = \begin{cases} 0, t < 0 \\ 1, t > 0 \end{cases} . \tag{2.1.2}$$

In our cases this is always assumed to be true. Thus, the linear response function is always given by

$$p(t) = \int_0^\infty d\tau \alpha(\tau) E(t - \tau) . \tag{2.1.3}$$

A convolution of two functions f and g is given as [17, p.206]

$$\{f * g\}(t) = \int_{-\infty}^{\infty} d\tau f(\tau) g(t - \tau) = \int_{-\infty}^{\infty} d\tau f(t - \tau) g(\tau) . \tag{2.1.4}$$

The convolution theorem states that the Fourier transform of a convolution in the time domain is the product of the Fourier transform of the functions [17, p.223]

$$\mathcal{F}[f * g] = \mathcal{F}[f]\mathcal{F}[g] , \tag{2.1.5}$$

and similarly an Fourier transform of a product of two functions is a convolution of their Fourier transforms [17, p.223]

$$\mathcal{F}[fg] = \mathcal{F}[f] * \mathcal{F}[g] . \tag{2.1.6}$$

Using this relation, the Fourier transform of equation (2.1.3)

$$p(\omega) = \alpha(\omega) E(\omega) , \tag{2.1.7}$$

which shows that it is often easier to work with responses in the frequency domain as we mainly do.

The Heaviside step function's Fourier transform reads [18]

$$\mathcal{F}[\theta](\omega) = \lim_{\varepsilon \to 0} \left[\frac{1}{\omega + i\varepsilon} = \mathcal{P}\frac{i}{\omega} + \pi\delta(\omega) \right] , \tag{2.1.8}$$

where $\mathcal{P}$ represents the Cauchy principal value [19, p.403]. This means that, when integrating

over the function which has a pole at x, one takes the limit

$$\lim_{\varepsilon\to 0}\int_a^{x-\varepsilon} f(t)dt + \int_{x+\varepsilon}^{b} f(t)dt\,, \tag{2.1.9}$$

and with infinite integration bounds, when a and/or $b = \infty$, one considers the limits

$$\lim_{r\to\infty}\int_{-r}^{r} f(t)dt,\ \lim_{r\to\infty}\int_{a}^{r} f(t)dt,\ \lim_{r\to\infty}\int_{-r}^{b} f(t)dt\,. \tag{2.1.10}$$

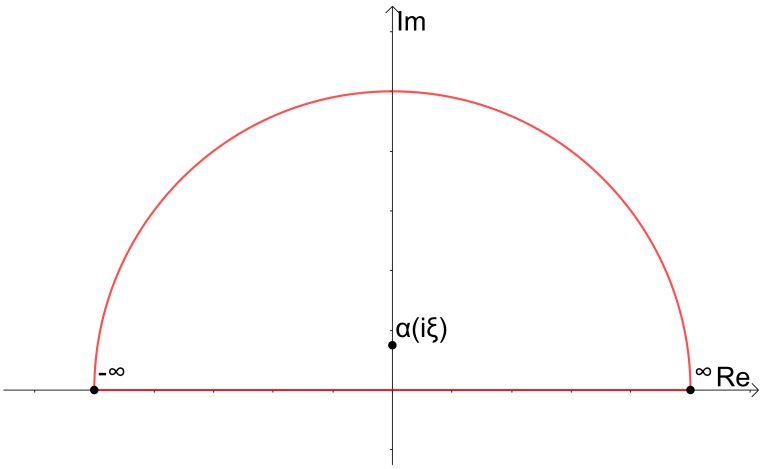

Figure 2.1: Integration path of the contour integration of $\alpha(\omega)$ used to find $\alpha(i\xi)$. The path goes conter clockwise along the real axis from $-\infty$ to ∞ and then around the upper half plane.

For causal response functions, the Kramers–Kronig relation makes it possible to find the imaginary part of a frequency domain response function by only knowing its real part and vice versa [18, 20, 21]. They are given by

$$\mathrm{Re}[\alpha(\omega)] = \frac{1}{\pi}\mathcal{P}\int_{-\infty}^{\infty}\frac{\mathrm{Im}[\alpha(\omega')]}{\omega'-\omega}d\omega'\,, \tag{2.1.11}$$

$$\mathrm{Im}[\alpha(\omega)] = -\frac{1}{\pi}\mathcal{P}\int_{-\infty}^{\infty}\frac{\mathrm{Re}[\alpha(\omega')]}{\omega'-\omega}d\omega'\,, \tag{2.1.12}$$

which can be obtained by applying the convolution theorem (2.1.5) to $\alpha(t) = \theta(t)Y(t)$, which yields [18]

$$\alpha(\omega) = \frac{1}{2\pi}\mathcal{P}\int_{-\infty}^{\infty}\frac{iY(\omega')}{\omega'-\omega} + \frac{Y(\omega)}{2}\,. \tag{2.1.13}$$

As one is free to choose $Y(t)$ for $t < 0$ one can set it first to $Y(-t) = Y(t)$. This yields that

$Y(\omega)$ is always real and one ends up with equation (2.1.11). If one sets $Y(-t) = -Y(t)$, one obtains equation (2.1.12). This derivation also shows that the Kramers–Kronig relations are equivalent to causality [18].

We can expect physical linear response functions to give real valued responses to any real external field. To achieve this effect, they have to obey the Schwartz reflection principle

$$\alpha(-\omega^*) = \alpha^*(\omega)\,, \tag{2.1.14}$$

and along the real axis this gives

$$\alpha(-\omega) = \alpha^*(\omega)\,. \tag{2.1.15}$$

In this way, the negative frequency part cancels out the imaginary response of the positive frequency part, without canceling the real response. Hence one can derive

$$\begin{aligned}\alpha(\omega) &= \frac{1}{\pi i}\mathcal{P}\int_{-\infty}^{\infty} d\omega' \frac{(\omega'+\omega)\alpha(\omega')}{(\omega'+\omega)(\omega'-\omega)} \\ &= \frac{2}{\pi}\mathcal{P}\int_{-\infty}^{\infty} d\omega' \frac{\omega' \operatorname{Im}[\alpha(\omega')]}{(\omega'^2-\omega^2)} - \frac{2i\omega}{\pi}\mathcal{P}\int_{-\infty}^{\infty} d\omega' \frac{\operatorname{Re}[\alpha(\omega')]}{(\omega'^2-\omega^2)}\,.\end{aligned} \tag{2.1.16}$$

which seperates into real and imaginary parts

$$\operatorname{Re}[\alpha(\omega)] = \frac{2}{\pi}\mathcal{P}\int_0^{\infty} d\omega' \frac{\omega' \operatorname{Im}[\alpha(\omega')]}{\omega'^2-\omega^2}\,, \tag{2.1.17}$$

and

$$\operatorname{Im}[\alpha(\omega)] = -\frac{2\omega}{\pi}\mathcal{P}\int_0^{\infty} d\omega' \frac{\operatorname{Re}[\alpha(\omega')]}{\omega'^2-\omega^2}\,. \tag{2.1.18}$$

By integrating $\frac{\alpha(\omega)}{\omega - i\xi}$ along the real axis and around the upper half-plane, where $\alpha(\omega) = 0$ as shown in figure 2.1, and assuming that $\alpha(\omega)$ is analytical in the upper half plane, that is there are no poles, one can apply the Cauchy's integral formula [19, pp.371-373].

The residue theorem states that a contour integral, that is an integral along a continuous line enclosing an area is equal to $2\pi i$ times the residue of the inside area. As our integral path is the limit of such a contour integral, and $\alpha(\omega) \to 0$ as $|\omega| \to \infty$ fast enough. Then Cauchy's integration formula gives us

$$\alpha(i\xi) = \frac{1}{2\pi i}\oint d\omega \frac{\alpha(\omega)}{\omega - i\xi} = \frac{1}{2\pi i}\int_{-\infty}^{\infty} d\omega \frac{\alpha(\omega)}{\omega - i\xi}\,. \tag{2.1.19}$$

Multiplying equation (2.1.19) by $\frac{\omega-i\xi}{\omega-i\xi}$, and using the Schwarz reflection principle (2.1.14), one finds

$$\alpha(i\xi) = \frac{1}{\pi}\int_0^\infty d\omega \frac{\omega\,\mathrm{Im}[\alpha(\omega)]}{\omega^2+\xi^2}\,, \tag{2.1.20}$$

transforming the imaginary part of the response function onto a real valued function. This form of the responce function will be used later for the calculation of of the dispersion interactions, see section 2.5.

2.2 Quantization of the Electromagnetic Field

Starting with the classical description of the electromagnetic field, we will derive a quantum theory of electromagnetism. We will see how we can describe the equations of motion of the electromagnetic fields compactly using Poisson brackets, the so-called Liouville equation, and then we will use the correspondence principle to quantize the fields to the Von-Neumann equation.

The classical electromagnetic fields are described by Maxwell equations: Gauss's law

$$\boldsymbol{\nabla}\cdot\boldsymbol{E}(\boldsymbol{r}) = \frac{\rho(\boldsymbol{r})}{\varepsilon_0}\,, \tag{2.2.1}$$

which relates charges $\boldsymbol{\rho}$ as sources for the electric field $\boldsymbol{E}$. Gauss's law for magnetism

$$\boldsymbol{\nabla}\cdot\boldsymbol{B}(\boldsymbol{r}) = 0\,, \tag{2.2.2}$$

which shows that the non-existence of magnetic monopoles, Faraday's law

$$\boldsymbol{\nabla}\times\boldsymbol{E}(\boldsymbol{r}) = -\dot{\boldsymbol{B}}(\boldsymbol{r})\,, \tag{2.2.3}$$

describing the induction of an electric field due to a changing magnetic field, $\boldsymbol{B}$, and Ampère's law

$$\boldsymbol{\nabla}\times\boldsymbol{B}(\boldsymbol{r}) = \mu_0\left[\boldsymbol{J}(\boldsymbol{r}) + \varepsilon_0\dot{\boldsymbol{E}}(\boldsymbol{r})\right]\,. \tag{2.2.4}$$

which relates currents $\boldsymbol{J}$ as magnetic field sources and describes the induction of magnetic fields due to changing electric fields. With the vacuum permittivity ε_0 and vacuum permeability μ_0. In vacuum, there are no currents or free charges and Maxwell equations turn

into

$$\boldsymbol{\nabla} \cdot \boldsymbol{E}(\boldsymbol{r}) = 0\,, \tag{2.2.5}$$

$$\boldsymbol{\nabla} \cdot \boldsymbol{B}(\boldsymbol{r}) = 0\,, \tag{2.2.6}$$

$$\boldsymbol{\nabla} \times \boldsymbol{E}(\boldsymbol{r}) = -\dot{\boldsymbol{B}}(\boldsymbol{r})\,, \tag{2.2.7}$$

$$\boldsymbol{\nabla} \times \boldsymbol{B}(\boldsymbol{r}) = \mu_0 \varepsilon_0 \dot{\boldsymbol{E}}(\boldsymbol{r})\,. \tag{2.2.8}$$

In order to quantize the fields we will first need to describe the fields in the Hamiltonian formalism. By introducing the vector potential $\boldsymbol{A}$ such that

$$\boldsymbol{E} = -\dot{\boldsymbol{A}}\,, \tag{2.2.9}$$

$$\boldsymbol{B} = \boldsymbol{\nabla} \times \boldsymbol{A}\,, \tag{2.2.10}$$

one can derive the classical Lagrangian description of electromagnetism. The Lagrangian density of the electromagnetic field in free space reads [22, p.33]

$$\mathcal{L} = \frac{\varepsilon_0}{2}\dot{\boldsymbol{A}}^2 - \frac{1}{2\mu_0}(\boldsymbol{\nabla} \times \boldsymbol{A})^2 = \frac{\varepsilon_0}{2}\boldsymbol{E}^2 - \frac{1}{2\mu_0}\boldsymbol{B}^2\,. \tag{2.2.11}$$

The Lagrangian is given by its volume integral

$$L = \int d^3 r \mathcal{L}\,. \tag{2.2.12}$$

In order to quantize the electromagnetic field according to the second quantization scheme, the canonical coordinates and momenta are required. The latter can be fund by applying the functional derivation of the Lagrangian with respect to $\boldsymbol{A}$ [22, p.30]

$$\begin{aligned} \Pi_k(\boldsymbol{r'}) &= \frac{\delta L}{\delta \dot{A}_k(\boldsymbol{r})}(\boldsymbol{r'}) \\ &= \lim_{h \to 0} \frac{L[\dot{A}_j(\boldsymbol{r'}) + h\delta^{\perp}_{jk}(\boldsymbol{r'} - \boldsymbol{r}), A_j(r')] - L[\dot{A}_j(\boldsymbol{r'}), A_j(\boldsymbol{r'})]}{h}\,. \end{aligned} \tag{2.2.13}$$

With the transverse δ-function [22, p.27-28]

$$\boldsymbol{\delta}^{\perp}(\boldsymbol{r}) = \boldsymbol{\delta}(\boldsymbol{r}) + \boldsymbol{\nabla} \otimes \boldsymbol{\nabla}\frac{1}{4\pi r} = \boldsymbol{\nabla} \times (\boldsymbol{\nabla} \times \mathbf{1})\frac{1}{4\pi r}\,, \tag{2.2.14}$$

with $\otimes$ being the tensor product and $\mathbf{1}$ being the unit matrix. It acts similarly to the Dirac

δ-function, but it only keeps the transverse part of the function

$$\int d^3r' \boldsymbol{\delta}^{\perp}(\boldsymbol{r}-\boldsymbol{r'}) \cdot \boldsymbol{F}(\boldsymbol{r'}) = \boldsymbol{F}^{\perp}(\boldsymbol{r}) \,, \tag{2.2.15}$$

the resulting canonical momenta for the electromagnetic field yields [22, p.34]

$$\boldsymbol{\Pi}(\boldsymbol{r}) = \varepsilon_0 \dot{\boldsymbol{A}}^{\perp}(\boldsymbol{r}) = \varepsilon_0 \boldsymbol{E}(\boldsymbol{r}). \tag{2.2.16}$$

Next, we apply a Legendre transform in order to obtain the Hamiltonian of the system, which reads

$$H = \int d^3r \dot{\boldsymbol{A}}(\boldsymbol{r}) \cdot \boldsymbol{\Pi}(\boldsymbol{r}) - L = \int d^3r \left(\frac{1}{2\varepsilon_0} \boldsymbol{\Pi}^2 + \frac{1}{2\mu_0} (\boldsymbol{\nabla} \times \boldsymbol{A})^2 \right) . \tag{2.2.17}$$

Concerning the second quantization scheme the Poisson bracket

$$\{f, g\} = \sum_k \left(\frac{\partial f}{\partial q_k} \frac{\partial g}{\partial p_k} - \frac{\partial f}{\partial p_k} \frac{\partial g}{\partial q_k} \right) , \tag{2.2.18}$$

are required. In the case of electromagnetic fields, they have to be applied in terms of functional derivatives like in (2.2.13). Hence, the definition of Poisson brackets reads

$$\{f, g\} = \int d^3r \left(\frac{\delta f}{\delta \boldsymbol{A}(\boldsymbol{r})} \frac{\delta g}{\delta \boldsymbol{\Pi}(\boldsymbol{r})} - \frac{\delta f}{\delta \boldsymbol{\Pi}(\boldsymbol{r})} \frac{\delta g}{\delta \boldsymbol{A}(\boldsymbol{r})} \right) . \tag{2.2.19}$$

The Poisson bracket has the property that it allows the Hamilton equations of motion to be written on the compact form as Liouville equations

$$\dot{\boldsymbol{A}}(\boldsymbol{r}) = \{\boldsymbol{A}(\boldsymbol{r}), H\} \,, \tag{2.2.20}$$

$$\dot{\boldsymbol{\Pi}}(\boldsymbol{r}) = \{\boldsymbol{\Pi}(\boldsymbol{r}), H\} \,, \tag{2.2.21}$$

We now impose the Coloumb gauge (transversal gauge)

$$\boldsymbol{\nabla} \cdot \boldsymbol{A}(\boldsymbol{r}, t) = 0 \,, \tag{2.2.22}$$

which means that there are only transverse parts left. In this gauge, the Poisson bracket of

the canonical momenta and coordinates reduces to

$$\{\boldsymbol{A}(\boldsymbol{r}), \boldsymbol{\Pi}(\boldsymbol{r'})\} = \delta^{\perp}(\boldsymbol{r} - \boldsymbol{r'})\,, \tag{2.2.23}$$

and the Poisson bracket of the electric and magnetic fields to

$$\{\boldsymbol{E}(\boldsymbol{r}), \boldsymbol{B}(\boldsymbol{r'})\} = \frac{1}{\varepsilon_0}\boldsymbol{\nabla} \times \delta^{\perp}(\boldsymbol{r} - \boldsymbol{r'})\,. \tag{2.2.24}$$

From (2.2.20) and (2.2.21), we obtain the Helmholtz equation

$$\ddot{\boldsymbol{A}}(\boldsymbol{r}, t) = \frac{1}{\varepsilon_0 \mu_0}\Delta \boldsymbol{A}(\boldsymbol{r}, t)\,, \tag{2.2.25}$$

which is equivalent to the wave equation

$$\Delta \boldsymbol{A}(\boldsymbol{r}, t) - \frac{1}{c^2}\ddot{\boldsymbol{A}}(\boldsymbol{r}, t) = 0\,, \tag{2.2.26}$$

with $c^2 = \frac{1}{\varepsilon_0 \mu_0}$ being the speed of light squared. By assuming $\boldsymbol{A}(\boldsymbol{r}, t) = \boldsymbol{A}(\boldsymbol{r})u(t)$, the wave equation (2.2.26) can be separated into its spatial and temporal part

$$\Delta \boldsymbol{A}_\lambda(\boldsymbol{r}) + \frac{\omega_\lambda^2}{c^2}\boldsymbol{A}_\lambda(\boldsymbol{r}) = 0\,, \tag{2.2.27}$$

$$u_\lambda(t) + \omega_\lambda^2 \ddot{u}_\lambda(t) = 0\,, \tag{2.2.28}$$

respectively. Equation (2.2.27) is equivalent to an eigenvalue equation of the Laplace operator, Δ, with eigenvalues $\frac{\omega_\lambda^2}{c^2}$ and eigenvectors $\boldsymbol{A}_\lambda$ Thus, the solutions $\{A_\lambda\}$ form a complete orthonormal set with normalization [7, p.682]

$$\int d^3 r \boldsymbol{A}_\lambda^*(\boldsymbol{r}) \cdot \boldsymbol{A}_{\lambda'}(\boldsymbol{r}) = \mathcal{N}_\lambda \delta_{\lambda\lambda'}\,, \tag{2.2.29}$$

and completeness

$$\sum_\lambda \frac{1}{\mathcal{N}_\lambda}\boldsymbol{A}_\lambda(\boldsymbol{r}) \otimes \boldsymbol{A}_\lambda^*(\boldsymbol{r'}) = \boldsymbol{\delta}^{\perp}(\boldsymbol{r} - \boldsymbol{r'})\,. \tag{2.2.30}$$

The solutions in Cartesian coordinates are plane waves $\boldsymbol{A}_\lambda(\boldsymbol{r}) = \boldsymbol{e}_\sigma(\boldsymbol{k})e^{i\boldsymbol{k}\cdot\boldsymbol{r}}$, where $k^2 = \frac{\omega_\lambda^2}{c^2}$ and $\boldsymbol{k} \cdot \boldsymbol{e}_\sigma = 0$. As we only have transverse components, there are two possible polarizations

for each $\boldsymbol{k}$. Thus, the mode summation becomes

$$\sum_{\lambda} \equiv \sum_{\sigma=1}^{2} \int \frac{d^3k}{(2\pi)^{3/2}} \,. \tag{2.2.31}$$

The temporal part reduces to a harmonic oscillator $\ddot{u}_\lambda(t) = u_\lambda e^{\pm i\omega_\lambda t}$. To this end, the entire solution reads

$$\boldsymbol{A}(\boldsymbol{r},t) = \sum_{\sigma=1}^{2} \int \frac{d^3k}{(2\pi)^{3/2}} \boldsymbol{e}_\sigma(\boldsymbol{k}) \left[u_{\boldsymbol{k}\sigma} e^{i(\boldsymbol{k}\cdot\boldsymbol{r}-\omega t)} + u^*_{\boldsymbol{k}\sigma} e^{-i(\boldsymbol{k}\cdot\boldsymbol{r}-\omega t)} \right] . \tag{2.2.32}$$

Using equation (2.2.32), the Hamiltonian (2.2.17) simplifies to [7, pp.682-683]

$$H = 2\varepsilon_0 \sum_{\sigma=1}^{2} \int d^3k \omega^2 |u_{\boldsymbol{k}\sigma}|^2 \,, \tag{2.2.33}$$

similar to the harmonic oscillator. By performing the canonical transfomation $q_{\boldsymbol{k}\sigma} = \sqrt{\varepsilon_0}(u_{\boldsymbol{k}\sigma} + u^*_{\boldsymbol{k}\sigma})$ and $p_{\boldsymbol{k}\sigma} = -i\omega\sqrt{\varepsilon_0}(u_{\boldsymbol{k}\sigma} - u^*_{\boldsymbol{k}\sigma})$, the Hamiltonian can be written as a harmonic oscillator

$$H = \frac{1}{2} \sum_{\sigma=1}^{2} \int d^3k (p^2_{\boldsymbol{k}\sigma} + \omega^2 q^2_{\boldsymbol{k}\sigma}) \,. \tag{2.2.34}$$

with generalized momenta $p_{\boldsymbol{k}\sigma}$ and coordinates $q_{\boldsymbol{k}\sigma}$. Thus, the fundamental Poisson bracket reads

$$\{q_{\boldsymbol{k}\sigma}, p_{\boldsymbol{k}'\sigma'}\} = \boldsymbol{\delta}^\perp(\boldsymbol{k} - \boldsymbol{k}')\delta_{\sigma\sigma'} \,. \tag{2.2.35}$$

We have now done all the required groundwork needed to perform the second quantization scheme. The correspondence principle describes how one can transform from a classical to a quantum theory by letting [22, p.35]

$$\{f, g\} \to \frac{1}{i\hbar}[\hat{f}, \hat{g}] \,, \tag{2.2.36}$$

which yields the commutator

$$[\hat{q}_{\boldsymbol{k}\sigma}, \hat{p}_{\boldsymbol{k}'\sigma'}] = i\hbar\boldsymbol{\delta}^\perp(\boldsymbol{k}' - \boldsymbol{k})\delta_{\sigma\sigma'} \,, \tag{2.2.37}$$

The complex amplitude functions with a new normalization now become

$$\hat{a}_\sigma(\boldsymbol{k}) = \sqrt{\frac{\omega}{2\hbar}}\left(\hat{q}_{\boldsymbol{k}\sigma} + \frac{i\hat{p}_{\boldsymbol{k}\sigma}}{\omega}\right), \quad \hat{a}^\dagger_\sigma(\boldsymbol{k}) = \sqrt{\frac{\omega}{2\hbar}}\left(\hat{q}_{\boldsymbol{k}\sigma} - \frac{i\hat{p}_{\boldsymbol{k}\sigma}}{\omega}\right), \tag{2.2.38}$$

with the commutator

$$[\hat{a}_\sigma(\boldsymbol{k}), \hat{a}'^\dagger_\sigma(\boldsymbol{k'})] = \delta(\boldsymbol{k} - \boldsymbol{k'})\delta_{\sigma\sigma'}\,, \tag{2.2.39}$$

and the vector potential operator results in

$$\hat{\boldsymbol{A}}(\boldsymbol{r}, t) = \sum_{\sigma=1}^{2}\int \frac{d^3k}{(2\pi)^{3/2}}\sqrt{\frac{\hbar}{2\varepsilon_0\omega}}\boldsymbol{e}_\sigma[e^{i(\boldsymbol{k}\cdot\boldsymbol{r}-\omega t)}\hat{a}_\sigma(\boldsymbol{k}) + e^{-i(\boldsymbol{k}\cdot\boldsymbol{r}-\omega t)}\hat{a}^\dagger_\sigma(\boldsymbol{k})]\,. \tag{2.2.40}$$

By formally Fourier transforming the field, we can write

$$\hat{\boldsymbol{A}}(\boldsymbol{r}) = \sum_\lambda [\boldsymbol{A}_\lambda(\boldsymbol{r})\hat{a}_\lambda + \boldsymbol{A}^*_\lambda(\boldsymbol{r})\hat{a}^\dagger_\lambda]\,, \tag{2.2.41}$$

with commutator

$$[\hat{a}_\lambda, \hat{a}^\dagger_{\lambda'}] = \delta_{\lambda\lambda'}\,. \tag{2.2.42}$$

The operators of the electric and magnetic fields become

$$\hat{\boldsymbol{E}}(\boldsymbol{r}) = i\sum_\lambda \omega_\lambda[\boldsymbol{A}_\lambda\hat{a}_\lambda - \boldsymbol{A}^*_\lambda\hat{a}^\dagger_\lambda]\,, \quad \hat{\boldsymbol{B}}(\boldsymbol{r}) = \sum_\lambda[\boldsymbol{\nabla}\times\boldsymbol{A}_\lambda\hat{a}_\lambda + \boldsymbol{\nabla}\times\boldsymbol{A}^*_\lambda\hat{a}^\dagger_\lambda]\,, \tag{2.2.43}$$

leading to the commutation relation

$$[\hat{\boldsymbol{E}}(\boldsymbol{r}), \hat{\boldsymbol{B}}(\boldsymbol{r'})] = -\frac{i\hbar}{\varepsilon_0}\boldsymbol{\nabla}\times\boldsymbol{\delta}^\perp(\boldsymbol{r} - \boldsymbol{r'})\,, \tag{2.2.44}$$

which is expected according to the correspondence principle, by adding the quantization scheme (2.2.36) to (2.2.24)

Inserting equation (2.2.41) into equation (2.2.17) the Hamiltonian operator becomes

$$\hat{H} = \frac{1}{2}\sum_\lambda \hbar\omega_\lambda(\hat{a}^\dagger_\lambda\hat{a}_\lambda + \hat{a}_\lambda\hat{a}^\dagger_\lambda) = \sum_\lambda \hbar\omega_\lambda\left(\hat{a}^\dagger_\lambda\hat{a}_\lambda + \frac{1}{2}\right). \tag{2.2.45}$$

This is the exact same Hamiltonian as for the quantum harmonic oscillator [23, p.5]. Defining

the number operator $\hat{N} = \sum_\lambda \hat{a}_\lambda^\dagger \hat{a}_\lambda$, we have that for any state $|\Psi\rangle$

$$\langle\Psi|\hat{N}|\Psi\rangle = \langle\Psi|\sum_\lambda \hat{a}_\lambda^\dagger \hat{a}_\lambda|\Psi\rangle = \sum_\lambda \langle a_\lambda\Psi|a_\lambda\Psi\rangle \geq 0\,. \tag{2.2.46}$$

Therefore there is a state $|0\rangle$, with the smallest non-negative eigenvalue, a_0, of $\hat{N}$. Due to the commutation relation (2.2.42) we find that

$$\hat{N}\hat{a}_\lambda|0\rangle = (a_0 - 1)\hat{a}_\lambda|0\rangle\,, \tag{2.2.47}$$

which contradicts the fact that $|0\rangle$ is the smallest eigenvalue unless $\hat{a}_\lambda|0\rangle = 0$. Thus, $a_0 = 0$. Similarly

$$\hat{N}\hat{a}_\lambda^\dagger|0\rangle = (a_0 + 1)\hat{a}_\lambda^\dagger|0\rangle = \hat{a}_\lambda^\dagger|0\rangle\,, \tag{2.2.48}$$

and

$$\hat{N}\hat{a}_\lambda^\dagger\hat{a}_{\lambda'}^\dagger|0\rangle = (1 + \hat{a}_\lambda^\dagger\hat{N})\hat{a}_{\lambda'}^\dagger|0\rangle = 2\hat{a}_\lambda^\dagger\hat{a}_{\lambda'}^\dagger|0\rangle\,. \tag{2.2.49}$$

One can show that the number operator spits out the number of $\hat{a}_\lambda^\dagger$ operators before the state $|0\rangle$ minus the number of $\hat{a}_\lambda$ operator [23, p.6]. For this reason, the operators $\hat{a}_\lambda^\dagger$ and $\hat{a}_\lambda$ are known as ladder operators and raising and lowering operators respectively.

These operators represent the creation and annihilation of photons. All bosonic fields have creation and annihilation operators with the commutation relation (2.2.42). Knowing this we see that the Hamiltonian is all the possible energies, $\hbar\omega_\lambda$, for the photons times the number of photons of that energy. The remaining infinite term $\sum_\lambda \frac{\hbar\omega_\lambda}{2}$ does not have a physical meaning, therefore we subtract it to remove it, and in doing so we change the Hamiltonian to [23, p.8]

$$\hat{H} = \sum_\lambda \hbar\omega_\lambda \hat{a}_\lambda^\dagger \hat{a}_\lambda\,. \tag{2.2.50}$$

This is our final Hamiltionian for the electromagnetic fields. From this we are able to find the equations of motions for the system. The commutator between canonical coordinate, $\hat{\boldsymbol{A}}(\boldsymbol{r},\omega)$, of the field the Hamiltonian gives the equation of motion for the canonical coordinate, the Von-Neumann equation reads

$$\left[\hat{\boldsymbol{A}}(\boldsymbol{r},\omega), \hat{H}\right] = \hbar\omega\hat{\boldsymbol{A}}(\boldsymbol{r},\omega)\,. \tag{2.2.51}$$

When we later redo this quantization in the presence of dielectric media, we would like our

new canonical coordinate to obey the same equation of motion.

2.3 Langevin Noise Approach

After the quantization of the electromagnetic fields in the vacuum, we would like to quantize them in the presence of absorbing magnetoelectric materials. To perform this quantization, we will use the Langevin noise approach [7, pp.710-719]. We begin with the macroscopic Maxwell equations in absorbing magnetoelectric materials in the absence of charges which reads

$$\boldsymbol{\nabla} \cdot \boldsymbol{B}(\boldsymbol{r}) = 0\,, \tag{2.3.1}$$

$$\boldsymbol{\nabla} \times \boldsymbol{E}(\boldsymbol{r}) = -\dot{\boldsymbol{B}}(\boldsymbol{r})\,, \tag{2.3.2}$$

$$\boldsymbol{\nabla} \cdot \boldsymbol{D}(\boldsymbol{r}) = 0\,, \tag{2.3.3}$$

$$\boldsymbol{\nabla} \times \boldsymbol{H}(\boldsymbol{r}) = \dot{\boldsymbol{D}}(\boldsymbol{r})\,, \tag{2.3.4}$$

with

$$\boldsymbol{D}(\boldsymbol{r}) = \varepsilon_0 \boldsymbol{E}(\boldsymbol{r}) + \boldsymbol{P}(\boldsymbol{r})\,, \tag{2.3.5}$$

$$\boldsymbol{H}(\boldsymbol{r}) = \frac{1}{\mu_0}\boldsymbol{B}(\boldsymbol{r}) - \boldsymbol{M}(\boldsymbol{r})\,. \tag{2.3.6}$$

$\boldsymbol{D}$ is known as electric displacement. The polarization field, $\boldsymbol{P}$, being the dipole moment per unit volume creates bound charges in the medium. They can be written out of Gauss's law by using $\boldsymbol{D}$ instead of $\boldsymbol{E}$. Analogously the field $\boldsymbol{H}$ takes into account bound currents due to the magnetization, $\boldsymbol{M}$, and allows for their removal from Ampère's law.

In general for linear absorbing magnetoelectrics, the polarization and magnetization can be described as [7, p.710]

$$\boldsymbol{P}(\boldsymbol{r}, t) = \varepsilon_0 \int_0^\infty d\tau \chi_e(\boldsymbol{r}, \tau) \boldsymbol{E}(\boldsymbol{r}, t-\tau) + \boldsymbol{P}_N(\boldsymbol{r}, t)\,, \tag{2.3.7}$$

and

$$\boldsymbol{H}(\boldsymbol{r}, t) = \frac{1}{\mu_0} \int_0^\infty d\tau \chi_m(\boldsymbol{r}, \tau) \boldsymbol{B}(\boldsymbol{r}, t-\tau) - \boldsymbol{M}_N(\boldsymbol{r}, t)\,. \tag{2.3.8}$$

$\boldsymbol{P}_N(\boldsymbol{r})$ and $\boldsymbol{M}_N(\boldsymbol{r})$ are the noise polarization and noise magnetization. They exist due to random fluctuations in the materials. $\chi_e(\boldsymbol{r}, \tau)$ and $\chi_m(\boldsymbol{r}, \tau)$ are the electric and magnetic susceptibility, respectively. As we don't want to work with convolutions, we apply the Fourier

transform with respect to time t of the polarization (2.3.7) and the magnetization (2.3.8), the displacement field (2.3.5) then becomes

$$\boldsymbol{D}(\boldsymbol{r},\omega) = \varepsilon_0\varepsilon(\boldsymbol{r},\omega)\boldsymbol{E}(\boldsymbol{r},\omega) + \boldsymbol{P}_N(\boldsymbol{r},\omega)\,, \tag{2.3.9}$$

and equation (2.3.6) becomes

$$\boldsymbol{H}(\boldsymbol{r},\omega) = \kappa_0\kappa(\boldsymbol{r},\omega)\boldsymbol{B}(\boldsymbol{r},\omega) - \boldsymbol{M}_N(\boldsymbol{r},\omega)\,. \tag{2.3.10}$$

with, $\kappa_0 = \frac{1}{\mu_0}$ and $\kappa = \frac{1}{\mu}$. $\varepsilon(\boldsymbol{r},\omega)$ is the relative permittivity and $\kappa(\boldsymbol{r},\omega)$ is the inverse relative permeability. They are given by

$$\varepsilon(\boldsymbol{r},\omega) = 1 + \int_0^\infty d\tau e^{i\omega\tau}\chi_e(\boldsymbol{r},\tau)\,, \tag{2.3.11}$$

and

$$\kappa(\boldsymbol{r},\omega) = 1 - \int_0^\infty d\tau e^{i\omega\tau}\chi_m(\boldsymbol{r},\tau)\,. \tag{2.3.12}$$

$\chi_e(\boldsymbol{r},\omega)$ and $\chi_m(\boldsymbol{r},\omega)$ are both linear response functions that obeys the Kramers–Kronig relations (2.1.17) and (2.1.18).

By inserting (2.3.9) and (2.3.10) into (2.3.1)-(2.3.4), and applies the temporal Fourier transform the Maxwell equations becomes

$$\boldsymbol{\nabla}\cdot\boldsymbol{B}(\boldsymbol{r},\omega) = 0\,, \tag{2.3.13}$$

$$\boldsymbol{\nabla}\times\boldsymbol{E}(\boldsymbol{r},\omega) = i\omega\boldsymbol{B}(\boldsymbol{r},\omega)\,, \tag{2.3.14}$$

$$\varepsilon_0\boldsymbol{\nabla}\cdot[\varepsilon(\boldsymbol{r},\omega)\boldsymbol{E}(\boldsymbol{r},\omega)] = \rho_N(\boldsymbol{r},\omega)\,, \tag{2.3.15}$$

$$\boldsymbol{\nabla}\times[\kappa(\boldsymbol{r},\omega)\boldsymbol{B}(\boldsymbol{r},\omega)] + i\frac{\omega}{c^2}\varepsilon(\boldsymbol{r},\omega)\boldsymbol{E}(\boldsymbol{r},\omega) = \mu_0\boldsymbol{j}_N(\boldsymbol{r},\omega)\,. \tag{2.3.16}$$

with the noise charge density

$$\rho_N(\boldsymbol{r},\omega) = -\boldsymbol{\nabla}\cdot\boldsymbol{P}_N(\boldsymbol{r},\omega)\,, \tag{2.3.17}$$

and the noise current density

$$\boldsymbol{j}_N(\boldsymbol{r},\omega) = -i\omega\boldsymbol{P}_N(\boldsymbol{r},\omega) + \boldsymbol{\nabla}\times\boldsymbol{M}_N(\boldsymbol{r},\omega)\,. \tag{2.3.18}$$

Inserting equation (2.3.14) into (2.3.16), one obtains the vector Helmholtz equation

$$\boldsymbol{\nabla} \times \boldsymbol{\nabla} \times \boldsymbol{E}(\boldsymbol{r}, \omega) - \frac{\omega^2}{c^2} \boldsymbol{E}(\boldsymbol{r}, \omega) = i\mu_0 \omega \boldsymbol{j}(\boldsymbol{r}, \omega)\,, \tag{2.3.19}$$

with

$$\boldsymbol{j}(\boldsymbol{r}, \omega) = \int d^3 r' \mathbf{Q}(\boldsymbol{r}, \boldsymbol{r'}, \omega) \cdot \boldsymbol{E}(\boldsymbol{r'}, \omega) + \boldsymbol{j}_N(\boldsymbol{r}, \omega)\,. \tag{2.3.20}$$

where $\mathbf{Q}(\boldsymbol{r}, \boldsymbol{r'}, \omega)$ is the complex conductivity tensor in the frequency domain. Both the effect of κ and ε are encodeed in $\mathbf{Q}(\boldsymbol{r}, \boldsymbol{r'}, \omega)$. The form of equation (2.3.20) is the most general linear response between the current density and the electric field. The conductivity tensor must be reciprocal [7, p.712]

$$\mathbf{Q}(\boldsymbol{r}, \boldsymbol{r'}, \omega) = \mathbf{Q}^T(\boldsymbol{r'}, \boldsymbol{r}, \omega)\,, \tag{2.3.21}$$

describing the inversion of optical paths. As it is a physical response function, we assume that $\mathbf{Q}(\boldsymbol{r}, \boldsymbol{r'}, t)$ being the temporal Fourier transform of $\mathbf{Q}(\boldsymbol{r}, \boldsymbol{r'}, \omega)$ is causal. We also assume that it is analytic in the upper half plane, satisfies the Kramers-Kronig relations and the Schwartz reflection principle (2.1.14)

$$\mathbf{Q}(\boldsymbol{r}, \boldsymbol{r'}, -\omega^*) = \mathbf{Q}^*(\boldsymbol{r}, \boldsymbol{r'}, \omega)\,, \tag{2.3.22}$$

which ensures we always have a real valued response. Inserting (2.3.20) into the Helmholtz equation (2.3.19), it generalizes to

$$\boldsymbol{\nabla} \times \boldsymbol{\nabla} \times \boldsymbol{E}(\boldsymbol{r}, \omega) - \frac{\omega^2}{c^2} \boldsymbol{E}(\boldsymbol{r}, \omega) - i\mu_0 \omega \int d^3 r' \mathbf{Q}(\boldsymbol{r}, \boldsymbol{r'}, \omega) \cdot \boldsymbol{E}(\boldsymbol{r'}, \omega) = i\mu_0 \omega \boldsymbol{j}_N(\boldsymbol{r}, \omega)\,, \tag{2.3.23}$$

which has an unique solution on the form

$$\boldsymbol{E}(\boldsymbol{r}, \omega) = i\mu_0 \omega \int d^3 r' \mathbf{G}(\boldsymbol{r}, \boldsymbol{r'}, \omega) \cdot \boldsymbol{j}_N(\boldsymbol{r'}, \omega)\,. \tag{2.3.24}$$

with the Green tensor $\mathbf{G}(\boldsymbol{r}, \boldsymbol{r'}, \omega)$ satisfying

$$\boldsymbol{\nabla} \times \boldsymbol{\nabla} \times \mathbf{G}(\boldsymbol{r}, \boldsymbol{s}, \omega) - \frac{\omega^2}{c^2} \mathbf{G}(\boldsymbol{r}, \boldsymbol{s}, \omega) - i\mu_0 \omega \int d^3 r' \mathbf{Q}(\boldsymbol{r}, \boldsymbol{r'}, \omega) \cdot \mathbf{G}(\boldsymbol{r'}, \boldsymbol{s}, \omega) = \boldsymbol{\delta}(\boldsymbol{r} - \boldsymbol{s})\,. \tag{2.3.25}$$

The Green tensor is the linear response of the electric field to external currents. Here in

the absence of charges, it reduces to the response of the noise currents. Later in section 3.1 we will see how the Green tensor represents the propagation of photons. The Green tensor being a linear response function, has all the properties of them, such as satisfying the Kramers–Kronig relations, the Schwartz reflection principle, and it is reciprocal (2.3.21).

Before we quantize the theory we would like to derive an important property of the Green tensor that will be used when we derive the Casimir–Polder potential in section 2.5. Equation (2.3.25) can equivalently be written as an integral equation

$$\int d^3s \mathbf{H}(\boldsymbol{r}, \boldsymbol{s}, \omega) \cdot \mathbf{G}(\boldsymbol{s}, \boldsymbol{r'}, \omega) = \boldsymbol{\delta}(\boldsymbol{r'} - \boldsymbol{r}), \tag{2.3.26}$$

with $\mathbf{H}(\boldsymbol{r}, \boldsymbol{s}, \omega)$ being reciprocal and equal to

$$\mathbf{H}(\boldsymbol{r}, \boldsymbol{r'}, \omega) = \boldsymbol{\nabla} \times \boldsymbol{\nabla} \times \boldsymbol{\delta}(\boldsymbol{r} - \boldsymbol{r'}) - \frac{\omega^2}{c^2}\boldsymbol{\delta}(\boldsymbol{r} - \boldsymbol{r'}) - i\mu_0\omega\mathbf{Q}(\boldsymbol{r}, \boldsymbol{r'}, \omega). \tag{2.3.27}$$

The complex conjugate of equation (2.3.26) reads

$$\int d^3s \mathbf{G}^\dagger(\boldsymbol{s}, \boldsymbol{r}, \omega) \cdot \mathbf{H}^\dagger(\boldsymbol{s}, \boldsymbol{r'}, \omega) = \boldsymbol{\delta}(\boldsymbol{r} - \boldsymbol{r'})\,. \tag{2.3.28}$$

Multiplying equation (2.3.26) with $\mathbf{G}^\dagger(\boldsymbol{s'}, \boldsymbol{r}, \omega)$ and integrate over $\boldsymbol{r}$, results in

$$\int d^3r \int d^3s \mathbf{G}^\dagger(\boldsymbol{s'}, \boldsymbol{r}, \omega) \cdot \mathbf{H}(\boldsymbol{r}, \boldsymbol{s}, \omega) \cdot \mathbf{G}(\boldsymbol{s}, \boldsymbol{r'}, \omega) = \mathbf{G}^\dagger(\boldsymbol{s'}, \boldsymbol{r'}, \omega)\,. \tag{2.3.29}$$

Then multiplying equation (2.3.28) with $\mathbf{G}(\boldsymbol{r'}, \boldsymbol{s'}, \omega)$ from the right and integrate over $\boldsymbol{r'}$, results in

$$\int d^3r' \int d^3s \mathbf{G}^\dagger(\boldsymbol{s}, \boldsymbol{r}, \omega) \cdot \mathbf{H}^\dagger(\boldsymbol{s}, \boldsymbol{r'}, \omega) \cdot \mathbf{G}(\boldsymbol{r'}, \boldsymbol{s'}, \omega) = \mathbf{G}(\boldsymbol{r'}, \boldsymbol{s'}, \omega)\,. \tag{2.3.30}$$

By renaming the integration variables and taking the difference of these two equations yields the Green identity

$$\mu_0\omega \int d^3s \int d^3s' \mathbf{G}(\boldsymbol{r}, \boldsymbol{s}, \omega) \cdot \boldsymbol{\sigma}(\boldsymbol{s}, \boldsymbol{s'}, \omega) \cdot \mathbf{G}^\dagger(\boldsymbol{s'}, \boldsymbol{r'}, \omega) = \operatorname{Im} \mathbf{G}(\boldsymbol{r}, \boldsymbol{r'}, \omega)\,, \tag{2.3.31}$$

with

$$\boldsymbol{\sigma}(\boldsymbol{s}, \boldsymbol{s'}, \omega) = \operatorname{Re} \boldsymbol{Q}(\boldsymbol{s}, \boldsymbol{s'}, \omega)\,. \tag{2.3.32}$$

We formally define the "square root" of $\boldsymbol{\sigma}$ as

$$\boldsymbol{\sigma}(\boldsymbol{r},\boldsymbol{r'},\omega) = \int d^3s \mathbf{K}(\boldsymbol{r},\boldsymbol{s},\omega)\cdot\mathbf{K}^\dagger(\boldsymbol{r'},\boldsymbol{s},\omega)\,. \tag{2.3.33}$$

Now it is possible to quantize this theory using $\hat{\boldsymbol{j}}_N$ as our canonical coordinate. By using the correspondence principle on the Poisson bracket of the noise current with its complex conjugate, one finds the commutation relation [7, p.713]

$$\left[\hat{\boldsymbol{j}}_N(\boldsymbol{r},\omega),\hat{\boldsymbol{j}}_N^\dagger(\boldsymbol{r'},\omega')\right] = \frac{\hbar\omega}{\pi}\delta(\omega-\omega')\boldsymbol{\sigma}(\boldsymbol{r},\boldsymbol{r'},\omega)\,. \tag{2.3.34}$$

By formally defining a new field operator $\hat{\boldsymbol{f}}(\boldsymbol{r},\omega)$ such that

$$\hat{\boldsymbol{j}}_N(\boldsymbol{r},\omega) = \left(\frac{\hbar\omega}{\pi}\right)^{1/2}\int d^3r'\mathbf{K}(\boldsymbol{r},\boldsymbol{r'},\omega)\cdot\hat{\boldsymbol{f}}(\boldsymbol{r'},\omega)\,, \tag{2.3.35}$$

the field $\hat{\boldsymbol{f}}$ satisfies the bosonic field commutator (2.2.42)

$$\left[\hat{\boldsymbol{f}}(\boldsymbol{r},\omega),\hat{\boldsymbol{f}}^\dagger(\boldsymbol{r'},\omega')\right] = \delta(\omega-\omega')\boldsymbol{\delta}(\boldsymbol{r}-\boldsymbol{r'})\,. \tag{2.3.36}$$

As $\hat{\boldsymbol{j}}(\boldsymbol{r},\omega)$ is our canonical coordinate, we want a Hamiltonian that gives the same equation of motion as with the quantized electromagnetic fields earlier(2.2.51)

$$\left[\hat{\boldsymbol{j}}_N(\boldsymbol{r},\omega),\hat{H}\right] = \hbar\omega\hat{\boldsymbol{j}}_N(\boldsymbol{r},\omega)\,. \tag{2.3.37}$$

In order to achieve this goal the Hamiltonian must be of the form

$$\hat{H} = \pi\int_0^\infty d\omega\int d^3r\int d^3r\hat{\boldsymbol{j}}_N^\dagger(\boldsymbol{r},\omega)\cdot\boldsymbol{\rho}(\boldsymbol{r},\boldsymbol{r'},\omega)\cdot\hat{\boldsymbol{j}}_N(\boldsymbol{r'},\omega)\,, \tag{2.3.38}$$

with $\boldsymbol{\rho}(\boldsymbol{r},\boldsymbol{r'},\omega)$ being the inverse of $\boldsymbol{\sigma}(\boldsymbol{r},\boldsymbol{r'},\omega)$. To this end, in terms of $\hat{\boldsymbol{f}}(\boldsymbol{r},\omega)$, the Hamiltonian reads

$$\hat{H} = \pi\int_0^\infty d\omega\int d^3r\,\hbar\omega\hat{\boldsymbol{f}}^\dagger(\boldsymbol{r},\omega)\cdot\hat{\boldsymbol{f}}(\boldsymbol{r},\omega)\,. \tag{2.3.39}$$

The form of this Hamiltonian is very similar to the form of the free-space Hamiltonian. We once again have the number operator times the energy of the quanta of the field $\hat{\boldsymbol{f}}$, created and annihilated by the $\hat{\boldsymbol{f}}$ and $\hat{\boldsymbol{f}}^\dagger$ operators. These represent the analog to the photons in this field theory. They are not only photons but also the polarization of the dielectric material.

However, we will later refer to the operators as creating and annihilating photons, even though this does not capture the entire picture. It is now possible to write the operators for $\boldsymbol{E}(\boldsymbol{r},\omega)$ and $\boldsymbol{B}(\boldsymbol{r},\omega)$ in terms of $\hat{\boldsymbol{f}}(\boldsymbol{r},\omega)$. We will need it later in order to find the coupling between the spheres and the electric field. The electric field operator becomes

$$\hat{\boldsymbol{E}}(\boldsymbol{r},\omega) = i\mu_0\omega\sqrt{\frac{\hbar\omega}{\pi}}\int d^3r' \int d^3s \mathbf{G}(\boldsymbol{r},\boldsymbol{r'},\omega)\cdot\mathbf{K}(\boldsymbol{r'},\boldsymbol{s},\omega)\cdot\hat{\boldsymbol{f}}(\boldsymbol{s},\omega)\,, \tag{2.3.40}$$

and

$$\hat{\boldsymbol{E}}(\boldsymbol{r}) = \int_0^\infty d\omega \hat{\boldsymbol{E}}(\boldsymbol{r},\omega) + \text{h.c.} \tag{2.3.41}$$

Analogously the magnetic field operator becomes

$$\hat{\boldsymbol{B}}(\boldsymbol{r},\omega) = \mu_0\sqrt{\frac{\hbar\omega}{\pi}}\boldsymbol{\nabla}\times\int d^3r' \mathbf{G}(\boldsymbol{r},\boldsymbol{r'},\omega)\cdot\mathbf{K}(\boldsymbol{r'},\boldsymbol{s},\omega)\cdot\hat{\boldsymbol{f}}(\boldsymbol{s},\omega) \tag{2.3.42}$$

and

$$\hat{\boldsymbol{B}}(\boldsymbol{r}) = \int_0^\infty d\omega \hat{\boldsymbol{B}}(\boldsymbol{r},\omega) + \text{h.c.} \tag{2.3.43}$$

The equal time commutation relation for the electric and magnetic field is

$$\begin{aligned}\left[\hat{\boldsymbol{E}}(\boldsymbol{r}),\hat{\boldsymbol{B}}(\boldsymbol{r'})\right] &= \frac{2i\hbar\mu_0}{\pi}\boldsymbol{\nabla}_{\boldsymbol{r'}}\times\int_0^\infty d\omega\,\omega\,\text{Im}\,\mathbf{G}(\boldsymbol{r},\boldsymbol{r'},\omega)\\ &= \frac{\hbar}{\pi\varepsilon_0 c^2}\boldsymbol{\nabla}_{\boldsymbol{r'}}\times\int_{-\infty}^\infty d\omega\,\omega\mathbf{G}(\boldsymbol{r},\boldsymbol{r'},\omega)\,.\end{aligned} \tag{2.3.44}$$

In the high frequency limit $\mathbf{G}(\boldsymbol{r},\boldsymbol{r'},\omega)\approx -\frac{c^2}{\omega^2}\boldsymbol{\delta}(\boldsymbol{r}-\boldsymbol{r'})$, and thus the equal time commutation relation becomes

$$\left[\hat{\boldsymbol{E}}(\boldsymbol{r}),\hat{\boldsymbol{B}}(\boldsymbol{r'})\right] = \frac{i\hbar}{\varepsilon_0}\boldsymbol{\nabla}\times\boldsymbol{\delta}^\perp(\boldsymbol{r}-\boldsymbol{r'})\,, \tag{2.3.45}$$

which is the same as in free space, see equation (2.2.44).

The case relevant for this thesis, is a medium with no magnetic response, that is spatially local

$$\boldsymbol{\sigma}(\boldsymbol{r},\boldsymbol{r'},\omega) = \boldsymbol{\sigma}(\boldsymbol{r},\omega)\delta(\boldsymbol{r}-\boldsymbol{r'})\,, \tag{2.3.46}$$

isotropic

$$\boldsymbol{\sigma}(\boldsymbol{r},\omega) = \sigma(\boldsymbol{r},\omega)\mathbf{1}\,, \tag{2.3.47}$$

and inhomogeneous. This leads to [7, p.715]

$$\sigma(\boldsymbol{r},\omega) = \varepsilon_0\omega\sqrt{\operatorname{Im}\chi(\boldsymbol{r},\omega)}\,. \tag{2.3.48}$$

Thus the electric field operator becomes

$$\hat{\boldsymbol{E}}(\boldsymbol{r},\omega) = i\sqrt{\frac{\hbar}{\pi\varepsilon_0}}\frac{\omega^2}{c^2}\int d^3r'\sqrt{\operatorname{Im}\chi(\boldsymbol{r'},\omega)}\mathbf{G}(\boldsymbol{r},\boldsymbol{r'},\omega)\cdot\hat{\boldsymbol{f}}(\boldsymbol{r'},\omega)\,, \tag{2.3.49}$$

where $\chi(\boldsymbol{r},\omega)$ is the electric susceptibility of the system.

2.4 Clausius–Mossotti relations

Now that we have a good description of the electromagnetic fields in our system, we will need to have a description of the coupling of the spheres to the electric field. To find this we will need its polarizability. Therefore, we would like to find a relationship between the permittivity of a sphere relative to the medium it is in, and its polarizability. The Clausius–Mossotti relation [24, p.168] gives that there is a relation between the atomic polarizability and the relative dielectric constant, for a dielectric sphere in a vacuum. This relationship can be derived by finding the electric field of a dielectric sphere in a medium, with an electric field that is homogeneous and equal to $E_0\boldsymbol{z}$ at long distances from the sphere. We consider a dielectric sphere of radius a, placed in another dielectric medium. The electric field is homogeneous with amplitude E_0 at large distances from the sphere. The sphere is made of a material with dielectric constant ε_1 in a surrounding medium with dielectric constant ε_2. Figure 2.2 illustrates the system. The derivation of the electric field is based on [25, pp.157-159].

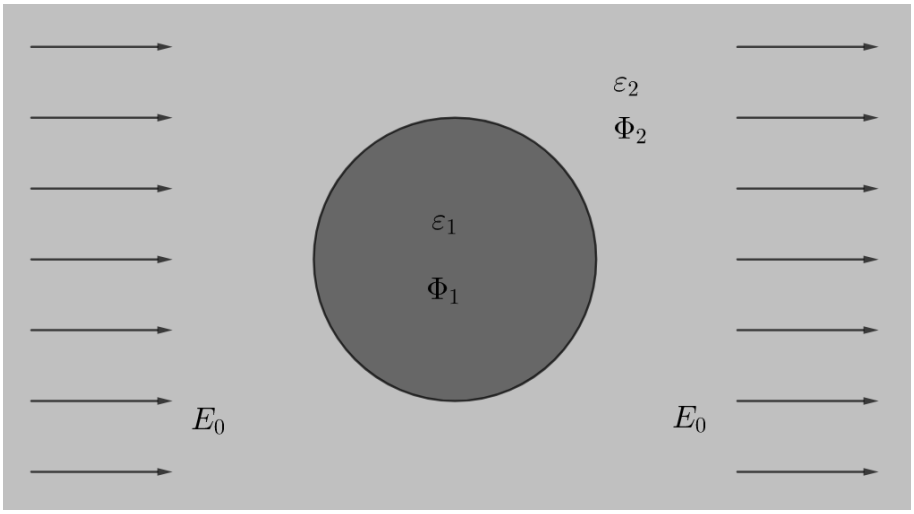

Figure 2.2: Dielectric sphere, ε_1, with radius a in dielectric medium, ε_2, with the potentials Φ_1 inside the sphere and Φ_2 outside it, as well as the electric field $\boldsymbol{E_0}$ at large distances.

One can use Maxwell's equations to solve for the electric field. Due to the absence of free charges or currents in the system, Gauss law becomes zero on the right side and gives

$$\boldsymbol{\nabla} \cdot \boldsymbol{E} = \mathbf{0}\,, \tag{2.4.1}$$

and Faradays law of induction becomes

$$\boldsymbol{\nabla} \times \boldsymbol{E} = \mathbf{0}\,. \tag{2.4.2}$$

This allows the equations to be written in terms of potentials, $\boldsymbol{\nabla}\Phi = -\boldsymbol{E}$, and one obtains the Laplace equation

$$\boldsymbol{\nabla}^2\Phi = 0\,. \tag{2.4.3}$$

Due to the geometry of the system, one can transform to spherical coordinates. It has azimuthal symmetry about the direction of the homogeneous field. Thus, the solutions to the Laplace equation is of the form

$$\Phi(r,\theta) = \sum_{l=0}^{\infty} \left[A_l r^l + \frac{B_l}{r^{l+1}} \right] P_l(\cos\theta)\,, \tag{2.4.4}$$

where $P_l(\cos\theta)$ is the l'th Legendre polynomial [26, p.142].

To avoid singularities, one assumes that inside the sphere the solution is of the form

$$\Phi_1(r,\theta) = \sum_{l=0}^{\infty} A_l r^l P_l(\cos\theta)\,, \tag{2.4.5}$$

and outside it is of the form

$$\Phi_2(r,\theta) = \sum_{l=0}^{\infty} \left[B_l r^l + \frac{C_l}{r^{l+1}} \right] P_l(\cos\theta)\,. \tag{2.4.6}$$

The scalar potential has to coincide with the external field far away from the sphere, $\Phi \to -E_0 r\cos\theta$. This yields $B_1 = -E_0$. All other B_l's have to vanish. Thus, the tangential Maxwell boundary conditions at the surface of the sphere yields

$$\frac{\partial\Phi_1}{\partial\theta}\Big|_{r=a} = \frac{\partial\Phi_2}{\partial\theta}\Big|_{r=a}\,, \tag{2.4.7}$$

and the normal yields

$$\varepsilon_1 \frac{\partial\Phi_1}{\partial r}\Big|_{r=a} = \varepsilon_2 \frac{\partial\Phi_2}{\partial r}\Big|_{r=a}\,. \tag{2.4.8}$$

Since all the Legendre polynomials are orthogonal the coefficients for each Legendre polynomial have to be equal separately, the tangential boundary conditions yields

$$A_1 = -E_0 + \frac{C_1}{a^3}\,, \tag{2.4.9}$$

and

$$A_l = \frac{C_l}{a^{l+2}},\ \text{for } l \neq 1\,. \tag{2.4.10}$$

The normal boundary conditions yields

$$(\varepsilon_1/\varepsilon_2)A_1 = -E_0 - 2\frac{C_l}{a^3}\,, \tag{2.4.11}$$

and

$$(\varepsilon_1/\varepsilon_2)A_l = -(l+1)\frac{C_l}{a^{l+2}}\,. \tag{2.4.12}$$

Hence, the solution of this system of equations reads

$$A_1 = -\left(\frac{3}{(\varepsilon_1/\varepsilon_2)+2}\right)E_0\,, \quad C_1 = \left(\frac{(\varepsilon_1/\varepsilon_2)-1}{(\varepsilon_1/\varepsilon_2)+2}\right)a^3 E_0\,, \tag{2.4.13}$$

and vanishes for all the remaining terms. Thus, the inside field is

$$\Phi_1 = -\left(\frac{3}{(\varepsilon_1/\varepsilon_2)+2}\right) E_0 r\cos\theta\,, \tag{2.4.14}$$

and the outside field is

$$\Phi_2 = -E_0 r\cos\theta + \left(\frac{(\varepsilon_1/\varepsilon_2)-1}{(\varepsilon_1/\varepsilon_2)+2}\right) E_0 \frac{a^3}{r^2}\cos\theta\,. \tag{2.4.15}$$

The inside field is a field parallel to the homogeneous field, but with a different magnitude, which is proportional to the dielectric constants. Outside of the sphere, the field separates into the uniform field and a dipole field with dipole moment

$$p = 4\pi\varepsilon_0\varepsilon_2\left(\frac{\varepsilon_1/\varepsilon_2 - 1}{\varepsilon_1/\varepsilon_2 + 2}\right) a^3 E_0\,. \tag{2.4.16}$$

By comparing equation (2.4.16) with an induced dipole moment $p = \alpha E$, we can identify a polarizability constant

$$\alpha = 4\pi\varepsilon_0\varepsilon_2\left(\frac{\varepsilon_1/\varepsilon_2 - 1}{\varepsilon_1/\varepsilon_2 + 2}\right) a^3\,. \tag{2.4.17}$$

As the permittivity of the mediums are linear response functions the polarizability also becomes a linear response function and can be written as

$$\alpha(\omega) = 4\pi\varepsilon_0\varepsilon_2(\omega)\left(\frac{\varepsilon_1(\omega)/\varepsilon_2(\omega) - 1}{\varepsilon_1(\omega)/\varepsilon_2(\omega) + 2}\right) a^3\,. \tag{2.4.18}$$

2.5 Casimir–Polder potential

In this section, we will show how the quantum fields give rise to forces between neutral atoms and dielectric bodies. This force is known as the Casimir–Polder force, as an example of a dispersion force [7, p.747]. We will follow the perturbative method. The derivation is based on [7, pp.751-753]. The magnetic coupling however, is much smaller than the electric, thus, we will restrict ourselves to the electric coupling. Pertubation theory is a method that allows for the approximation of a system where the Hamiltonian is of the form

$$\hat{H} = \hat{H}_0 + \hat{H}'\,, \tag{2.5.1}$$

where $\hat{H}_0$ is a Hamiltonian with a known set of orthonormal eigenfunctions $\{|I\rangle\}$. $\hat{H}'$ is a small pertubation of that system. The solution can then be written as a power series with eigenfunctions

$$|I\rangle = |0\rangle + |I\rangle_1 + |I\rangle_2 + \dots , \tag{2.5.2}$$

and eigenvalues

$$E_I = E_G + E_{I1} + E_{I2} + \dots . \tag{2.5.3}$$

The known Hamiltonian of our system is the atomic Hamiltonian and the electromagnetic field Hamiltonian (2.3.39). The eigenstates of the unperturbed system that we consider are the ground state $|0\rangle$ and the intermediate Fock states $|I\rangle = |k\rangle|\mathbf{1}_\lambda(\boldsymbol{r},\omega)\rangle$. These are the states where the atom is excited to the k-th energy level in the presence of a single field excitation $|\mathbf{1}_\lambda(\boldsymbol{r},\omega)\rangle = \hat{\boldsymbol{f}}^\dagger(\boldsymbol{r},\omega)|0\rangle$. The atom-field coupling Hamiltonian is given by [7, p.751]

$$\hat{H}_{AF} = -\hat{\boldsymbol{d}} \cdot \hat{\boldsymbol{E}}(\boldsymbol{r}_A) - \hat{\boldsymbol{m}} \cdot \hat{\boldsymbol{B}}(\boldsymbol{r}_A) , \tag{2.5.4}$$

however as the magnetic coupling is very weak we will only look at the dipole coupling and use

$$\hat{H}_{AF} = -\hat{\boldsymbol{d}} \cdot \hat{\boldsymbol{E}}(\boldsymbol{r}_A) . \tag{2.5.5}$$

We assume that our atoms are in the ground state, $|0\rangle$. Then the first order energy contribution vanishes

$$\Delta E = \langle 0|\hat{H}_{AF}|0\rangle = 0 , \tag{2.5.6}$$

as the Hamiltonian only describes transitions between energy states. The electric field operator $\hat{\boldsymbol{E}}(\boldsymbol{r}_A)$ annihilates and creates a photon, and the operator $\hat{\boldsymbol{d}}$ changes the atom from one state to another. The second order energy then becomes the leading order and it is given by

$$\Delta E = \sum_{I \neq G} \frac{\langle 0|\hat{H}_{AF}|I\rangle\langle I|\hat{H}_{AF}|0\rangle}{E_G - E_I} \neq 0 , \tag{2.5.7}$$

where G stands for the uncoupled ground state of the system, and I is the intermediate state where the atom is excited to some state ,$|k\rangle$, and there is a photon present ,$|\mathbf{1}_\lambda(\boldsymbol{r},\omega)\rangle$, thus $|I\rangle = |\mathbf{1}_\lambda(\boldsymbol{r},\omega)\rangle|k\rangle$. Due to the presence of excited states in the equation this gives a non-zero contributions to the energy. The matrix elements of the electric field interaction

becomes

$$\langle 0|\langle\{0\}|\hat{\boldsymbol{d}}\cdot\hat{\boldsymbol{E}}(\boldsymbol{r}_A)|\mathbf{1}_\lambda(\boldsymbol{r},\omega)\rangle|k\rangle = \sqrt{\frac{\hbar\omega}{\pi}}\int d^3r'\boldsymbol{d}_{0k}\cdot\mathbf{G}(\boldsymbol{r}_A,\boldsymbol{r},\omega)\cdot\mathbf{K}(\boldsymbol{r'},\boldsymbol{r},\omega)\,. \tag{2.5.8}$$

Inserting equation (2.5.8) into (2.5.7) and using Green identity (2.3.31) the resulting energy shift takes the form

$$\Delta E = -\frac{\mu_0}{\pi}\sum_k\int_0^\infty \frac{d\omega}{\omega_{k0}+\omega}\left[\omega^2\boldsymbol{d}_{0k}\cdot\operatorname{Im}\mathbf{G}(\boldsymbol{r}_A,\boldsymbol{r}_A,\omega)\cdot\boldsymbol{d}_{k0}\right]\,. \tag{2.5.9}$$

What we have calculated here is the self-interaction of the electrons in the neutral atom with the electric field. By inserting the free-space Green tensor we would arrive at what is known as the Lamb shift [23, p.187], which is a change in an atom's energy levels due to electron self-interaction. However, as we are surrounded by dielectric materials the equal position Green tensor, $\mathbf{G}(\boldsymbol{r}_A,\boldsymbol{r}_A,\omega)$ is not the same at all $\boldsymbol{r}_A$. Thus, we have found a position-dependent Lamb shift.

In section 3.1, we show that the Green tensor can be separated into a bulk and a scattering part. The Casimir–Polder potential is found by subtracting the position independent bulk part of the Green tensor, and shifting the integration to one along the imaginary frequency axis and then use the Schwartz reflection principle (2.1.14), which yields

$$U_e(\boldsymbol{r}_A) = \frac{\hbar\mu_0}{2\pi}\int_0^\infty d\xi\xi^2\alpha(i\xi)\operatorname{tr}\mathbf{G}^{(S)}(\boldsymbol{r}_A,\boldsymbol{r}_A,i\xi), \tag{2.5.10}$$

with the polarizability

$$\boldsymbol{\alpha}(\omega) = \lim_{\varepsilon\to0}\frac{2}{\hbar}\sum_k\frac{\omega_{k0}\boldsymbol{d}_{k0}\otimes\boldsymbol{d}_{k0}}{\omega_{0k}^2-\omega^2-i\omega\varepsilon}\,. \tag{2.5.11}$$

In summary, the Casimir–Polder potential (2.5.10) is the potential that arises due to the position-dependent energy shift caused by the presence of dielectric materials.

2.6 Thermal Casimir–Polder Forces

In the previous section, we introduced the Casimir–Polder potential at 0K. Now, we wish to include a finite temperature, and show how the addition of real thermal photons increases the magnitude of the Casimir–Polder potential. In thermal equilibrium, we can describe the

electromagnetic field with a density operator [7, p.718]

$$\hat{\varrho}_T = \frac{e^{-\hat{H}_F/(k_B T)}}{\mathrm{tr}\, e^{-\hat{H}_F/(k_B T)}}\,. \tag{2.6.1}$$

with [27, p.214]

$$\begin{aligned} e^{-\hat{H}_F/(k_B T)} = |0\rangle\langle 0| + \sum_{j=1}^{\infty} \int d^3 r_1 ... \int d^3 r_j \int_0^\infty d\omega_1 \int_0^\infty d\omega_j \\ \times\, e^{-\hbar(\omega_1 + ... + \omega_j)/(k_B T)} \\ \times\, |\mathbf{1}_{\lambda_1}(\boldsymbol{r}_1, \omega_1) ... \mathbf{1}_{\lambda_j}(\boldsymbol{r}_j, \omega_j)\rangle\langle \mathbf{1}_{\lambda_1}(\boldsymbol{r}_1, \omega_1) ... \mathbf{1}_{\lambda_j}(\boldsymbol{r}_j, \omega_j)|\,, \end{aligned} \tag{2.6.2}$$

and $\hat{H}_F$ being the electromagnetic field operator (2.3.39). The eigenstates of this operator are all states of the form $|\mathbf{1}_{\lambda_1}(\boldsymbol{r}_1, \omega_1) ... \mathbf{1}_{\lambda_j}(\boldsymbol{r}_j, \omega_j)\rangle$ and the vacuum ground state. The states $|\mathbf{1}_{\lambda_1}(\boldsymbol{r}_1, \omega_1) ... \mathbf{1}_{\lambda_j}(\boldsymbol{r}_j, \omega_j)\rangle$ are the same as $\hat{\boldsymbol{f}}^\dagger_{\lambda_1}(\boldsymbol{r}_1, \omega_1)\hat{\boldsymbol{f}}^\dagger_{\lambda_2}(\boldsymbol{r}_2, \omega_2) ... \hat{\boldsymbol{f}}^\dagger_{\lambda_j}(\boldsymbol{r}_j, \omega_j)|0\rangle$. These states represents states of j thermal photons. The eigenvalues of the operator represents the probability of having the thermal photons in this specific state be the measured thermal photons. Its result is that there are now real thermal photons in the system.

When taking two states $|a\rangle$ and $|b\rangle$, $\langle a|\hat{H}_{AF}|b\rangle$ is only non-zero when $|a\rangle$ and $|b\rangle$ have different atomic states, and they differ by one and only one photon. Thus, the energy shift from the first order perturbation energy term remains 0. If we still assume the atoms to be in their ground state, the expected second order perturbation energy term becomes

$$\langle \Delta E \rangle = \sum_{\psi} p_\psi \sum_{I \neq \psi} \frac{\langle \psi|\hat{H}_{AF}|I\rangle\langle I|\hat{H}_{AF}|\psi\rangle}{E_\Psi - E_I}\,, \tag{2.6.3}$$

with the non-zero terms states being

$$|I\rangle = |k\rangle|\mathbf{1}_{\lambda_1}(\boldsymbol{r}_1, \omega_1) ... \mathbf{1}_{\lambda_{j+1}}(\boldsymbol{r}_{j+1}, \omega_{j+1})\rangle\,, \tag{2.6.4}$$

and

$$|I\rangle = |k\rangle|\mathbf{1}_{\lambda_1}(\boldsymbol{r}_1, \omega_1) ... \mathbf{1}_{\lambda_{j-1}}(\boldsymbol{r}_{j-1}, \omega_{j-1})\rangle\,, \tag{2.6.5}$$

being the intermediate states, where the atom becomes excited to some higher energy level

by emitting or absorbing one photon, and

$$|\psi\rangle = |0\rangle|\mathbf{1}_{\lambda_1}(\boldsymbol{r}_1,\omega_1)...\mathbf{1}_{\lambda_j}(\boldsymbol{r}_j,\omega_j)\rangle\,, \tag{2.6.6}$$

being the states, where the atom is in its ground state surrounded by a thermal eigenstate. We have that $j \in \{0,1,2,...\}$, $\boldsymbol{r}_i \in \mathbb{R}^3$ and $\omega_i \in [0,\infty)$, with p_ψ being the probability of being in that state, found by the eigenvalue of the density operator. The resulting non-resonant Casimir–Polder potential is then given by [27, p.216]

$$U_{\mathrm{CP}}(\boldsymbol{r}_A) = \frac{\mu_0}{\pi}\sum_k \int_0^\infty d\omega\,\omega^2 \left[\frac{n(\omega)}{\omega+\omega_{0k}} - \frac{n(\omega)+1}{\omega-\omega_{0k}}\right] \boldsymbol{d}_{0k}\cdot \mathrm{Im}\,\mathbf{G}(\boldsymbol{r}_A,\boldsymbol{r}_A,\omega)\cdot\boldsymbol{d}_{k0}\,, \tag{2.6.7}$$

with the photon number distribution

$$n(\omega) = \frac{1}{e^{\hbar\omega/(k_BT)}-1}\,. \tag{2.6.8}$$

There are also resonant effects contributing to the Casimir–Polder potential [27, p.218]. For our purposes these are ignored. They do become relevant for excited atoms. Using that $n(-\omega) = -[n(\omega)+1]$ and that $\mathbf{G}(\boldsymbol{r}_A,\boldsymbol{r}_A,-\omega) = \mathbf{G}^*(\boldsymbol{r}_A,\boldsymbol{r}_A,\omega)$, one finds that

$$U_{\mathrm{CP}}(\boldsymbol{r}_A) = \frac{\mu_0}{\pi}\sum_k \mathcal{P}\int_{-\infty}^\infty d\omega\,\omega^2 \left[\frac{n(\omega)}{\omega+\omega_{0k}} - \frac{n(\omega)+1}{\omega-\omega_{0k}}\right] \boldsymbol{d}_{0k}\cdot \mathbf{G}(\boldsymbol{r}_A,\boldsymbol{r}_A,\omega)\cdot\boldsymbol{d}_{k0}\,, \tag{2.6.9}$$

This integral can be carried out by applying a principal-value contour integral along the real axis and around the upper half plane, leading to infinitesimally small semi-circle integrals around the poles at $\pm\omega_{0k}$, leading to the resonant Casimir–Polder potential, and 0, being the 0-th Matsubara frequency. There are several poles inside this contour along the imaginary axis at the Matsubara frequencies

$$\xi_j = \frac{2\pi k_BT}{\hbar}j,\;\; j = 0,1,2,3,\ldots\,. \tag{2.6.10}$$

An illustarion of the contour integral is given in figure 2.3. We will ignore the contribution from the resonant frequencies ω_{0k} and only consider the contribution from the inside poles and 0, which are known as the non-resonant contribution. Thus, the resulting potential is

$$U_{\mathrm{CP}}(r) = \mu_0 k_BT {\sum_{j=0}^\infty}' \xi_j^2\,\mathrm{tr}\left[\boldsymbol{\alpha}(i\xi_j)\cdot\mathbf{G}^{(S)}(\boldsymbol{r}_A,\boldsymbol{r}_A,i\xi_j)\right]\,, \tag{2.6.11}$$

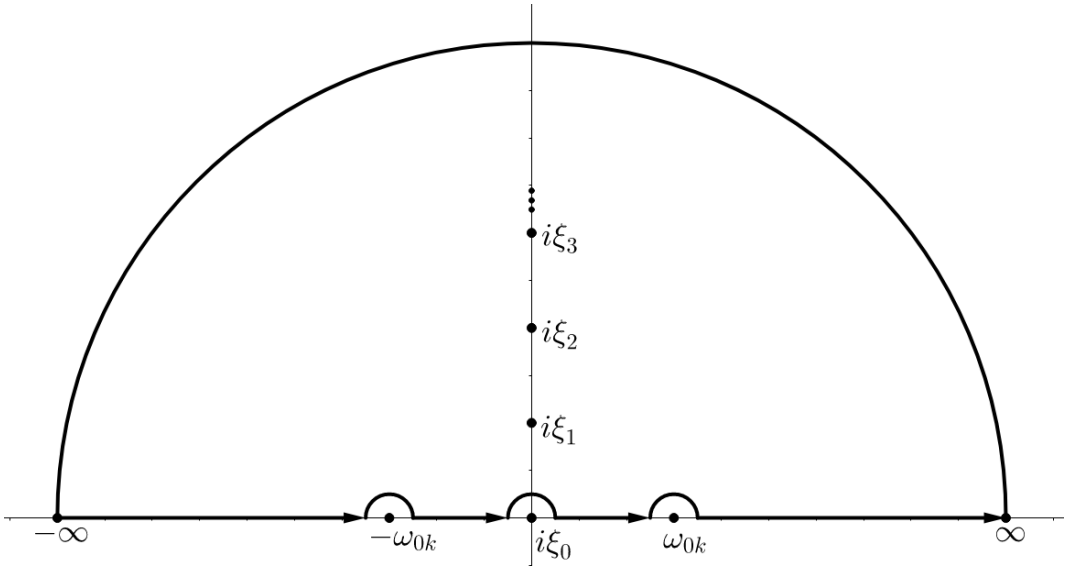

Figure 2.3: Contour integral path used for calculating the thermal Casimir–Polder potential. The path goes in infinitessimal semi-circles around the points 0 and $\pm\omega_{0k}$, representing the resonant frequencies, which we ignore. The first few poles at the Matsubara frequencies $i\xi_j$ are shown along the imaginary frequency axis.

where $\sum'$ means that the 0-th term is multiplied by $\frac{1}{2}$, as only a half-circle around ξ_0 is being integrated around. This potential is similar to the 0K Casimir–Polder potential, however, it scales with temperature, and it also only depends on the Matsubara frequencies, which grow further apart from each other as the temperature increases. After we find expressions for the polarizability and the Green tensor we will see that the expression being summed over in equation (2.6.11) is strictly decreasing as a function of $i\xi_j$, thus, increasing the temperature always leads to a stronger Casimir–Polder potential, as one would intuitively expect when more thermal photons are involved.

Chapter 3

Derivation of Trapping Frequencies

Having derived the theory of the forces involved we can start to apply them to our system. This chapter aims to go through the calculations of the trapping frequencies of spheres trapped in an optical potential in a hollow-core cylindrical fiber, surrounded by different mixtures of gases. First, the Born series expansion is discussed as a method to obtain a Green tensor approximation. Then, oscillator models for the permittivity and polarizability of gases and solids are discussed and sources for their values are given. This allows us to calculate the trapping frequencies using a Taylor series expansion of the potentials.

3.1 The Green Tensor

To find the Casimir–Polder potential inside the cylinder, the Green tensor describing the propagation of electromagnetic waves within our system is required. We find this by calculating the bulk media Green tensor of an arbitrary gas mixture, and then approximating the cylinder's Green tensor by employing a Born series expansion. We will see that the Green tensor can be thought of as representing the propagation of the photons through the medium, and how they scatter off the walls of the cylinder. We will also see how the dielectric functions of the gases change the value of the Green tensor.

We assume the gas in the cylinder is homogeneous and isotropic. Thus, the Green tensor can only depend on the relative coordinate $\boldsymbol{\rho} = \boldsymbol{r} - \boldsymbol{r'}$. We also assume, there is no magnetic response, that yields $\mu(\omega) = 1$. Due to isotropy and homogeity of the system, we can use Fourier transforms to solve the vector Helmholtz equation (2.3.25) [7, p.792]. The Fourier

transform of the Green tensor inside the hollow-core of the cylinder reads

$$\mathbf{G}(\boldsymbol{k},\omega) = \int \frac{d^3r}{(2\pi)^{3/2}} \mathbf{G}(\boldsymbol{\rho},\omega) e^{-i\boldsymbol{k}\cdot\boldsymbol{\rho}}\,, \tag{3.1.1}$$

and the Fourier transform of the Helmholtz equation reads

$$-\boldsymbol{k}\times\boldsymbol{k}\times\mathbf{G}(\boldsymbol{k},\omega) - \frac{\omega^2}{c^2}\varepsilon_{\text{gas}}(\omega)\mathbf{G}(\boldsymbol{k},\omega) = \mathbf{I}\,, \tag{3.1.2}$$

with the 3-dimensional unit matrix $\mathbf{I}$. This decomposes into the projection perpendicular and parallel to the wave vector $\boldsymbol{k}$

$$\mathbf{I} = \left(\mathbf{I} - \frac{\boldsymbol{k}\otimes\boldsymbol{k}}{k^2}\right) + \frac{\boldsymbol{k}\otimes\boldsymbol{k}}{k^2}\,. \tag{3.1.3}$$

By using the identity

$$-\boldsymbol{k}\times\boldsymbol{k}\times = k^2\left(\mathbf{I} - \frac{\boldsymbol{k}\otimes\boldsymbol{k}}{k^2}\right)\,, \tag{3.1.4}$$

the inside Green tensor becomes [7, p.793]

$$\begin{aligned}\mathbf{G}(\boldsymbol{\rho},\omega) = \int \frac{d^3k}{(2\pi)^{3/2}} e^{i\boldsymbol{k}\cdot\boldsymbol{\rho}} \left[\frac{c^2}{k^2c^2-\omega^2\varepsilon_{\text{gas}}(\omega)}\left(\mathbf{I}-\frac{\boldsymbol{k}\otimes\boldsymbol{k}}{k^2}\right) + \frac{c^2}{\omega^2\varepsilon_{\text{gas}}(\omega)}\frac{\boldsymbol{k}\otimes\boldsymbol{k}}{k^2}\right] \\ = \left[\boldsymbol{\nabla}\otimes\boldsymbol{\nabla} + q^2(\omega)\mathbf{I}\right]\frac{e^{iq(\omega)\rho}}{4\pi q^2(\omega)\rho}\,,\end{aligned} \tag{3.1.5}$$

with $q(\omega)^2 = \frac{\omega^2}{c^2}\varepsilon_{\text{gas}}(\omega)$. By carrying out the derivatives, the Green tensor reads

$$\mathbf{G}^{(0)}(\boldsymbol{\rho},\omega) = -\frac{\boldsymbol{\delta}(\boldsymbol{\rho})}{3q^2} + \frac{qe^{iq\rho}}{4\pi}\left[f\left(\frac{1}{q\rho}\right)\mathbf{I} - g\left(\frac{1}{q\rho}\right)\frac{\boldsymbol{\rho}\otimes\boldsymbol{\rho}}{\rho^2}\right]\,, \tag{3.1.6}$$

with

$$f(\mathrm{x}) = \mathrm{x} + \mathrm{i}\mathrm{x}^2 - \mathrm{x}^3\,, \tag{3.1.7}$$

and

$$g(\mathrm{x}) = \mathrm{x} + 3\mathrm{i}\mathrm{x}^2 - 3\mathrm{x}^3\,. \tag{3.1.8}$$

The full Green tensor consists of a bulk part, that is the same as inside the cylinder, and a scattering part

$$\mathbf{G}(\boldsymbol{r}_A,\boldsymbol{r}_A,\omega) = \mathbf{G}^{(0)}(\boldsymbol{r}_A,\boldsymbol{r}_A,\omega) + \boldsymbol{G}^{(S)}(\boldsymbol{r}_A,\boldsymbol{r}_A,\omega)\,. \tag{3.1.9}$$

We will approximate the scattering Green tensor inside the cylinder using the Born series expansion [7, p.800]. The bulk part of the full Green tensor solves the Helmholtz equation

$$\boldsymbol{\nabla} \times \boldsymbol{\nabla} \times \mathbf{G}^{(0)}(\boldsymbol{r}, \boldsymbol{r'}, \omega) - \frac{\omega^2}{c^2} \varepsilon_{\text{gas}}(\boldsymbol{r}, \omega) \mathbf{G}^{(0)}(\boldsymbol{r}, \boldsymbol{r'}, \omega) = \boldsymbol{\delta}(\boldsymbol{r} - \boldsymbol{r'}) \,, \tag{3.1.10}$$

and the full Green tensor solves

$$\boldsymbol{\nabla} \times \boldsymbol{\nabla} \times \mathbf{G}(\boldsymbol{r}, \boldsymbol{r'}, \omega) - \frac{\omega^2}{c^2} \varepsilon(\boldsymbol{r}, \omega) \mathbf{G}(\boldsymbol{r}, \boldsymbol{r'}, \omega) = \boldsymbol{\delta}(\boldsymbol{r} - \boldsymbol{r'}) \,, \tag{3.1.11}$$

for any field point $\boldsymbol{r}$ and source point $\boldsymbol{r'}$. Subtracting these two equations from each other, one arrives at [7, p.800]

$$\begin{aligned} &\boldsymbol{\nabla} \times \boldsymbol{\nabla} \times \mathbf{G}^{(S)}(\boldsymbol{r}, \boldsymbol{r'}, \omega) - \frac{\omega^2}{c^2} \varepsilon_{\text{gas}}(\boldsymbol{r}, \omega) \mathbf{G}^{(S)}(\boldsymbol{r}, \boldsymbol{r'}, \omega) = \\ &\frac{\omega^2}{c^2} \delta\varepsilon(\boldsymbol{r}, \omega) [\mathbf{G}^{(0)}(\boldsymbol{r}, \boldsymbol{r'}, \omega) + \mathbf{G}^{(S)}(\boldsymbol{r}, \boldsymbol{r'}, \omega)] \,, \end{aligned} \tag{3.1.12}$$

with

$$\delta\varepsilon(\boldsymbol{r}, \omega) = \varepsilon(\boldsymbol{r}, \omega) - \varepsilon_{\text{gas}}(\boldsymbol{r}, \omega) \,, \tag{3.1.13}$$

which gives

$$\begin{aligned} \delta\varepsilon(\boldsymbol{r}, \omega) = \varepsilon_{\text{wall}}(\boldsymbol{r}, \omega) - \varepsilon_{\text{gas}}(\boldsymbol{r}, \omega), &\qquad \text{for points in the wall,} \\ \delta\varepsilon(\boldsymbol{r}, \omega) = 0, &\qquad \text{for points outside the wall.} \end{aligned} \tag{3.1.14}$$

This differential equation is equivalent to the integral equation

$$\mathbf{G}^{(S)}(\boldsymbol{r}, \boldsymbol{r'}, \omega) = \int d^3s \mathbf{G}^{(0)}(\boldsymbol{r}, \boldsymbol{s}, \omega) \cdot \frac{\omega^2}{c^2} \delta\varepsilon(\boldsymbol{s}, \omega) [\mathbf{G}^{(0)}(\boldsymbol{s}, \boldsymbol{r'}, \omega) + \mathbf{G}^{(S)}(\boldsymbol{s}, \boldsymbol{r'}, \omega)] \,, \tag{3.1.15}$$

which can be solved iteratively via [7, p.801]

$$\begin{aligned} &\mathbf{G}^{(S)}(\boldsymbol{r}, \boldsymbol{r'}, \omega) = \frac{\omega^2}{c^2} \int d^3s' \mathbf{G}^{(0)}(\boldsymbol{r}, \boldsymbol{r'}, \omega) \delta\varepsilon(\boldsymbol{s'}, \omega) \mathbf{G}^{(0)}(\boldsymbol{s'}, \boldsymbol{r'}, \omega) \\ &+ \left(\frac{\omega^2}{c^2}\right)^2 \int d^3s' \int d^3s'' \mathbf{G}^{(0)}(\boldsymbol{r}, \boldsymbol{s'}, \omega) \cdot \delta\varepsilon(\boldsymbol{s'}, \omega) \mathbf{G}^{(0)}(\boldsymbol{s'}, \boldsymbol{s''}, \omega) \cdot \delta\varepsilon(\boldsymbol{s''}, \omega) \mathbf{G}^{(0)}(\boldsymbol{s''}, \boldsymbol{r'}, \omega) \\ &+ ... \end{aligned} \tag{3.1.16}$$

This is the Born series expansion. It can be understood as finding the Green tensor by first

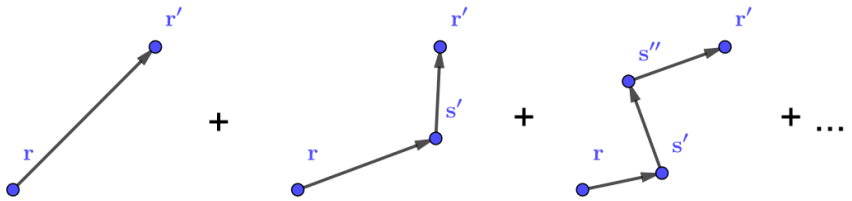

Figure 3.1: Diagram representation of the Born series expansion, showing how one considers the direct propagation from $\boldsymbol{r}$ to $\boldsymbol{r}'$ as well as propagation through $\boldsymbol{s}'$, $\boldsymbol{s}'$ and $\boldsymbol{s}''$, and so on.

considering a propagation from $\boldsymbol{r}$ to $\boldsymbol{r}'$ without scattering, then scattering once at some $\boldsymbol{s}'$, then at some $\boldsymbol{s}''$ and again at some $\boldsymbol{s}'''$ and so on as illustrated in figure 3.1. Thus, it is an expression in terms of scattering events. This is the context in which we can interpret the Green tensor as describing the propagation of the photons, and in this context, it is sometimes referred to as the propagator [28, p.396].

The bulk Green tensor consists of a singular part

$$\mathbf{D} = -\frac{\boldsymbol{\delta}(\boldsymbol{r})}{3q^2}\,, \tag{3.1.17}$$

and a regular part

$$\mathbf{R} = \frac{qe^{iq\rho}}{4\pi}\left[f\left(\frac{1}{q\rho}\right)\mathbf{I} - g\left(\frac{1}{q\rho}\right)\frac{\boldsymbol{\rho}\otimes\boldsymbol{\rho}}{\rho^2}\right]\,. \tag{3.1.18}$$

Inside the hollow center of the cylinder, the part of Born series expansion of the same point Green tensor, which only have two $\mathbf{R}$ terms are

$$\mathbf{G}^{(1)}(\boldsymbol{r},\boldsymbol{r},\omega) = \frac{\omega^2}{c^2}\int d^3s\,\delta\varepsilon(\boldsymbol{s},\omega)\sum_{n=0}^{\infty}\left(\frac{\delta\varepsilon(\boldsymbol{s},\omega)}{3\varepsilon_{\text{gas}}(\boldsymbol{s},\omega)}\right)^n \mathbf{R}(\boldsymbol{r},\boldsymbol{s},\omega)\cdot\mathbf{R}(\boldsymbol{s},\boldsymbol{r},\omega)\,. \tag{3.1.19}$$

The infinite series inside can be solved and by changing the integration volume to where $\delta\varepsilon(\boldsymbol{r},\omega)$ is non-zero and we obtain

$$\mathbf{G}^{(1)}(\boldsymbol{r},\boldsymbol{r},\omega) = \frac{\omega^2}{c^2}\frac{3\varepsilon_{\text{gas}}(\omega)\delta\varepsilon(\omega)}{3\varepsilon_{\text{gas}}(\omega)-\delta\varepsilon(\omega)}\int_V d^3s\mathbf{R}(\boldsymbol{r},\boldsymbol{s},\omega)\cdot\mathbf{R}(\boldsymbol{s},\boldsymbol{r},\omega)\,. \tag{3.1.20}$$

By taking the trace and switching to imaginary frequencies, such that $q \to i\zeta = i\frac{\xi}{c}\sqrt{\varepsilon(i\xi)}$,

we find

$$\operatorname{tr}\mathbf{G}^{(1)}(\boldsymbol{r},\boldsymbol{r},i\xi)=-\frac{\xi^2}{c^2}\frac{3\varepsilon_{\text{gas}}(i\xi)\delta\varepsilon(i\xi)}{3\varepsilon_{\text{gas}}(i\xi)-\delta\varepsilon(i\xi)}\int_V d^3s\frac{e^{-2\rho\zeta}}{8\pi^2\zeta^4\rho^6}\left[\zeta^4\rho^4+2\zeta^3\rho^3+5\zeta^2\rho^2+6\zeta\rho+3\right]\,. \tag{3.1.21}$$

This scattering Green tensor essentially represents the propagation of virtual photons in the intermediate states $|I\rangle$ being sent out from the electrons in the atoms in the sphere, through the gas mixture scattering of the cylinder wall once, and coming back to the atoms to be reabsorbed by their electrons.

3.2 Gas Permittivity and Sphere Polarizability Models

In this section, we explain the different models used to calculate the permittivity of gas mixtures and the polarizability of the spheres as functions of imaginary frequency. Different sources give approximations of these in different forms, and this section describes the methods used here.

In references [29] and [11], the polarizability of single gas molecules is approximated by an oscillator model [29]

$$\alpha(i\xi)=\sum_j\frac{\alpha_j}{1+(\xi/\omega_j)^2}\,. \tag{3.2.1}$$

The parameters for the polarizability strengths α_j and resonance frequencies ω_j are given in tables in reference [29] and [11]. From reference [29] we use the values for CO_2, CH_4, O_3, O_2, CO, NO_2 and H_2S, and in reference [11] we find the values for N_2O, NO and N_2

To find the permittivity of a mixture of gases we need the polarization per volume unit. We assume the mixture to be an ideal gas, such that the number of molecules per volume area is

$$\frac{N}{V}=\frac{P}{k_BT}\,. \tag{3.2.2}$$

The per volume polarizability thus reads

$$\tilde{\alpha}(i\xi)=\frac{P\alpha(i\xi)}{k_BT}\,. \tag{3.2.3}$$

With multiple gases in a mixture we can weight the contribution by their partial pressures

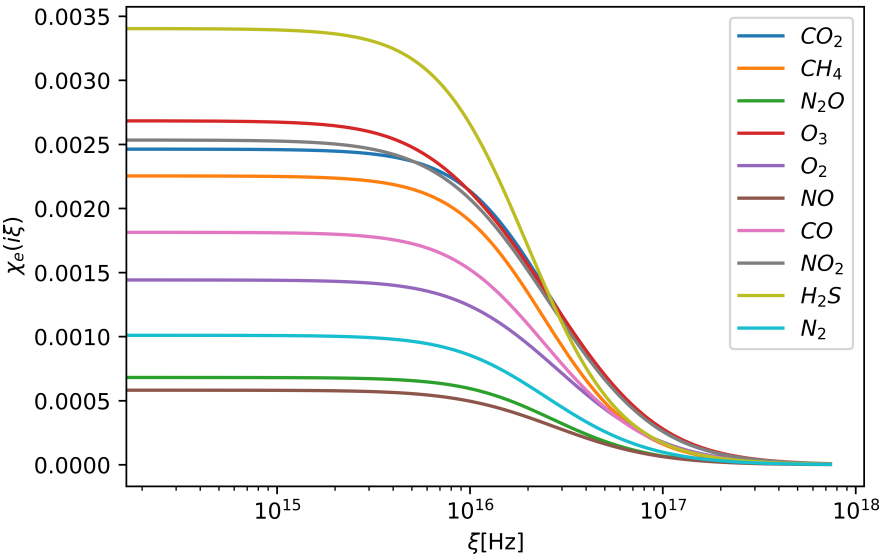

Figure 3.2: Plot of electric susceptibility, $\chi_e(i\xi) = \varepsilon(i\xi) - 1$ as a function of imaginary frequency ξ[Hz] for gases used at 300K and atmospheric pressure. The gases shown are CO_2 (blue), CH_4 (orange), N_2O (green), O_3 (red), O_2 (purple), NO (brown), CO (pink), NO_2 (gray), H_2S (olive) and N_2 (cyan).

P_i to find the polarizability of the mixture [30]

$$\tilde{\alpha}_{\text{mix}} = \sum_i \frac{P_i \alpha_i(i\xi)}{k_B T} \,. \tag{3.2.4}$$

The permittivity is then calculated from the Clausius–Mossotti relation(2.4.18)

$$\varepsilon_{\text{mix}} = \frac{1 + 2\tilde{\alpha}}{1 - \tilde{\alpha}} \,. \tag{3.2.5}$$

For the single gases, at imaginary frequencies, the dielectric functions $\varepsilon(i\xi)$ are depicted in figure 3.2. We see that they all take different values and that they are always decreasing until they flatten out at high energies at a value of one, which means that every material is transparent for high energy light.

The polarizability of most of the spheres is calculated using similar oscillator models or tabled data and Kramers–Kronig transforms(2.1.20) for finding the permittivity and then using the Clausius–Mossotti relation (2.4.18) to find the polarizability.

For the permittivity of the SiO_2 wall of the cylinder, a two oscillator model was used,

which reads [14]

$$\varepsilon(i\xi) = 1 + \frac{\omega_{P,1}^2}{\omega_{T,1}^2 + \gamma_1\xi + \xi^2} + \frac{\omega_{P,2}^2}{\omega_{T,2}^2 + \gamma_2\xi + \xi^2}\,, \tag{3.2.6}$$

where the applied parameters $\omega_{P,1}$, $\omega_{T,1}$, $\omega_{P,2}$, $\omega_{T,2}$, γ_1 and γ_2 can be found in in reference [14]. Generalizing to more oscillators this becomes

$$\varepsilon(i\xi) = 1 + \sum_i \frac{\omega_{P,i}^2}{\omega_{T,i}^2 + \gamma_i\xi + \xi^2}\,, \tag{3.2.7}$$

The corresponding parameters $\omega_{P,i}$, $\omega_{T,i}$ and γ_i for Mica, Gold and Rutile can be found in reference [31]. Using a similar oscillator model without damping

$$\varepsilon(i\xi) = 1 + \sum_i \frac{C_i}{1 + (\xi/\omega_i)^2}\,, \tag{3.2.8}$$

we find the permittivity of polytetrafluorethylene (PTFE), Silica and Polystyrene in reference [32].

The permittivities for the remaining materials can be obtained from tabled refraction n and extinction k measurements, which are related to permittivity via [33, p.7]

$$\varepsilon(\omega) = (n(\omega) + ik(\omega))^2\,. \tag{3.2.9}$$

These materials are gallium arsenide, α-Silicon, germanium, sodium Chloride and iridium and their mesurements are given in [33, pp.434, 575, 471, 781, 298]. Using the Kramers–Kronig transformation (2.1.20) on the permittivities of these materials, the imaginary frequency permittivity can be calculated

$$\varepsilon(i\xi) = \frac{1}{\pi}\int_0^\infty d\omega \frac{\omega\,\mathrm{Im}(\varepsilon(\omega))}{\omega^2 + \xi^2} + 1\,. \tag{3.2.10}$$

We then find the polarizability, $\alpha(i\xi)$ by using the Clausius–Mossotti relation (2.4.18) on these materials to relate it with the gas mixture's permittivity $\varepsilon_{\mathrm{gas}}(i\xi)$ the resulting polarizabilities read

$$\alpha(\omega) = 4\pi\varepsilon_0\varepsilon_{\mathrm{gas}}(\omega)\left(\frac{\varepsilon(\omega)/\varepsilon_{\mathrm{gas}}(\omega) - 1}{\varepsilon(\omega)/\varepsilon_{\mathrm{gas}}(\omega) + 2}\right)a^3\,. \tag{3.2.11}$$

Figure 3.3 illustrates the spectral behavior of these functions in along the imaginary frequency line. We see that they are all different and strictly decreasing, and at high frequencies they

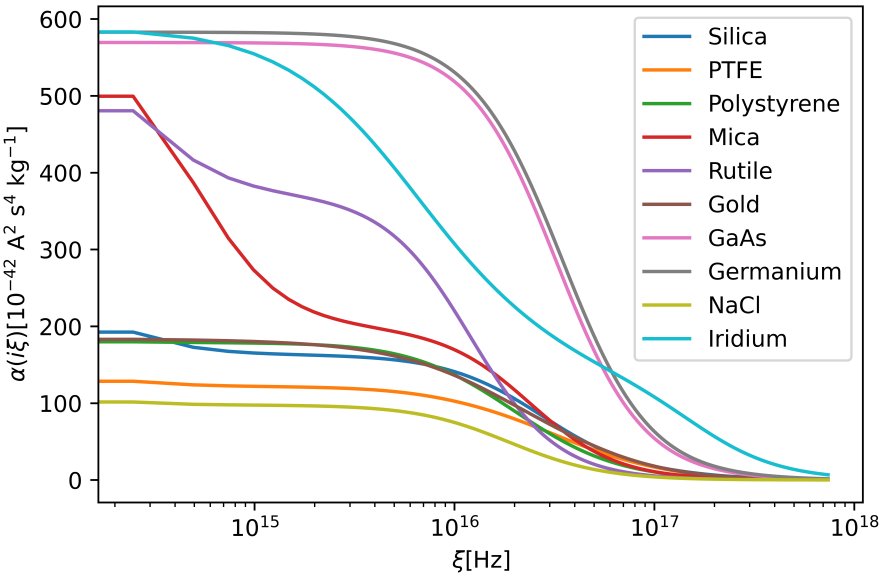

Figure 3.3: Plot of polarizability, $\alpha(i\xi)[10^{-42}\ \mathrm{A}^2\ \mathrm{s}^4\ \mathrm{kg}^{-1}]$ for r=10 nm spheres of different materials in a vacuum as a function of imaginary frequency, ξ[Hz]. The materials plotted are Silica (blue), PTFE(orange), Polystyrene (green), Mica (red), Rutile (purple), Gold (brown), Gallium Arsenide (pink), Germanium (grey), Sodium Chloride (olive) and Iridium (cyan).

go towards 0.

With both the Green tensor, the polarizabilities, and the permittivities known, the Casimir–Polder potential can be found by inserting them into equation (2.6.11). Our cylinder has a 1000 nm radius and a 500 nm hollow core. For simplicity, we will assume all spheres have a radius of 10 nm. In a vacuum, the Casimir–Polder potential of a SiO_2 sphere is plotted in figure 3.4.

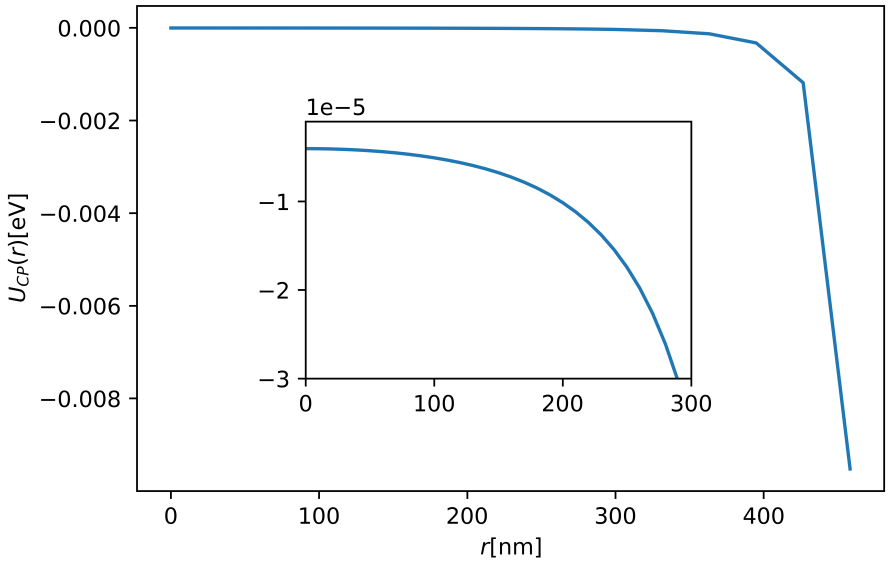

Figure 3.4: Casimir–Polder potential $U_{\mathrm{CP}}(r)$ as a function of r inside the hollow core for a radius = 10 nm SiO_2 sphere in a vacuum. The interval from 0 nm to 458 nm is shown, the inset shows the interval form 0 nm to 300 nm.

In the plot, we see that the energy change is smallest in the center and diverges towards $-\infty$ as it approaches the wall. Thus, we have a force pulling the spheres towards the wall.

3.3 Trapping Frequencies

For the training of the network, we need to calculate the trapping frequency of the spheres trapped in an optical potential

$$U_{\mathrm{optical}} = -\frac{1}{2}\alpha(\omega)E^2(\omega)\,, \tag{3.3.1}$$

superposed by the Casimir–Polder potential. Assuming the spheres oscillate near the center of the cylinder, where the first derivative of the Casimir–Polder potential(2.6.11), and the optical potential (3.3.1), of the potential is 0 due to symmetry, the frequency can be approximated using a harmonic oscillator model. Using $\boldsymbol{F} = m\boldsymbol{a}$ and Taylor expanding the derivative of the potential one finds

$$m\ddot{\boldsymbol{r}} = -\boldsymbol{r}\frac{\partial^2}{\partial \boldsymbol{r}^2}\left[U_{\mathrm{optical}}(\boldsymbol{0}) + U_{\mathrm{CP}}(\boldsymbol{0})\right]\,. \tag{3.3.2}$$

Due to the cylindrical symmetries of the problem, we see that the trapping frequnecy results in two unique frequencies per sphere, one along the radial axis of the cylinder, r, and one along the length of the cylinder, z given by

$$\omega_r = \sqrt{\frac{\partial_r^2 U_{\text{optical}} + \partial_r^2 U_{\text{CP}}}{m}}\,, \tag{3.3.3}$$

and

$$\omega_z = \sqrt{\frac{\partial_z^2 U_{\text{optical}}}{m}}\,. \tag{3.3.4}$$

As we only need the second derivative of the optical potential at the center of the cylinder, a very simple model for the laser field is chosen. It is assumed to be a standing laser field where the amplitude of $\boldsymbol{E}(\boldsymbol{r})$ drops off like a Gaussian curve from the center and is a cosine function along the length of the cylinder

$$E(\boldsymbol{r}) = E_0 e^{-2r^2/R^2} \cos\frac{\omega z}{c}\,, \tag{3.3.5}$$

with R being the $1/e^2$ radius of the laser beam. The resulting double derivatives of U_{optical} is then

$$\partial_r^2 U_{\text{optical}}(\mathbf{0}) = E_0^2 \alpha(\omega)\frac{2}{R^2}\,, \tag{3.3.6}$$

and

$$\partial_z^2 U_{\text{optical}}(\mathbf{0}) = E_0^2 \alpha(\omega)\frac{\omega^2}{c^2}\,. \tag{3.3.7}$$

With a laser field with a power of 0.0015 nW, a $1/\text{e}^2$ radius of 493.25 nm and a wavelength of 895 nm this was achieved. This is a weaker and thinner beam compared to the beam of the same wavelength in reference [34]. Choosing these parameters, we satisfy that the field does not penetrate the fiber, which would induce high-order effects. This is also chosen so that the optical double derivative in the radial direction $\partial_r^2 U_{\text{optical}}$, would always be stronger than the Casimir–Polder potentials double derivative, ensuring that the spheres remain trapped around the center. The change due to the Casimir–Polder potential is given in equation (2.6.11) and its double derivative with respect to r is

$$\partial_r^2 U_{\text{CP}}(0) = \mu_0 k_B T {\sum_{j=0}^{\infty}}' \xi_j^2 \alpha(i\xi_j)\partial_r^2 \operatorname{tr} \mathbf{G}^{(S)}(\mathbf{0},\mathbf{0},\xi_j)\,, \tag{3.3.8}$$

with

$$\begin{aligned}\partial_r^2 \operatorname{tr} \mathbf{G}^{(S)}(\mathbf{0},\mathbf{0},i\xi) = &-\frac{\xi^2}{c^2}\frac{3\varepsilon_{\text{gas}}(i\xi)\delta\varepsilon(i\xi)}{3\varepsilon_{\text{gas}}(i\xi)-\delta\varepsilon(i\xi)} \\ &\times \partial_r^2 \int_V d^3s \frac{e^{-2\rho\zeta}}{8\pi^2\zeta^4\rho^6}\left[\zeta^4\rho^4+2\zeta^3\rho^3+5\zeta^2\rho^2+6\zeta\rho+3\right] .\end{aligned} \tag{3.3.9}$$

By defining $f(\rho,\zeta)$ to be the function under the integral, and by using $\boldsymbol{s}=(s,z,\theta)$, and $\rho=|\boldsymbol{r}-\boldsymbol{s}|=\sqrt{r^2+z^2+s^2 2rs\cos\theta}$, and that $r=0$, we find

$$\begin{aligned}\partial_r^2 \operatorname{tr} \mathbf{G}^{(S)}(\mathbf{0},\mathbf{0},i\xi) = &-\frac{\xi^2}{c^2}\frac{3\varepsilon_{\text{gas}}(i\xi)\delta\varepsilon(i\xi)}{3\varepsilon_{\text{gas}}(i\xi)-\delta\varepsilon(i\xi)} \\ &\times \int_V d^3s \left(\frac{1}{\rho}\partial_\rho - \frac{s^2\cos^2\theta}{\rho^3}\partial_\rho + \frac{s^2\cos^2\theta}{\rho^2}\partial_\rho^2\right) f(\rho,\zeta) ,\end{aligned} \tag{3.3.10}$$

which yields

$$\begin{aligned}\partial_r^2 \operatorname{tr} \mathbf{G}^{(S)}(\mathbf{0},\mathbf{0},i\xi) = &-\frac{\xi^2}{c^2}\frac{3\varepsilon_{\text{gas}}(i\xi)\delta\varepsilon(i\xi)}{3\varepsilon_{\text{gas}}(i\xi)-\delta\varepsilon(i\xi)} \int_V d^3s \frac{e^{-2\rho\zeta}}{4\pi^2} \\ &\times \left[-\left(\frac{9}{\rho^8\zeta^4}+\frac{18}{\rho^7\zeta^3}+\frac{16}{\rho^6\zeta^2}+\frac{8}{\rho^5\zeta}+\frac{3}{\rho^4}+\frac{\zeta}{\rho^8}\right)\right. \\ &\left.+\, s^2\cos^2\theta\left(\frac{72}{\rho^{10}\zeta^4}+\frac{144}{\rho^9\zeta^3}+\frac{132}{\rho^8\zeta^2}+\frac{72}{\rho^7\zeta}+\frac{28}{\rho^6}+\frac{9\zeta}{\rho^5}+\frac{2\zeta^2}{\rho^4}\right)\right] .\end{aligned} \tag{3.3.11}$$

Finally we define

$$\begin{aligned}I = \int_V d^3s \frac{e^{-2\rho\zeta}}{4\pi^2}&\left[-\left(\frac{9}{\rho^8\zeta^4}+\frac{18}{\rho^7\zeta^3}+\frac{16}{\rho^6\zeta^2}+\frac{8}{\rho^5\zeta}+\frac{3}{\rho^4}+\frac{\zeta}{\rho^8}\right)\right. \\ &\left.+\, s^2\cos^2\theta\left(\frac{72}{\rho^{10}\zeta^4}+\frac{144}{\rho^9\zeta^3}+\frac{132}{\rho^8\zeta^2}+\frac{72}{\rho^7\zeta}+\frac{28}{\rho^6}+\frac{9\zeta}{\rho^5}+\frac{2\zeta^2}{\rho^4}\right)\right] .\end{aligned} \tag{3.3.12}$$

As we are integrating at $r=0$, ρ is independent of θ. Thus we integrate the angular part of

the integral, where we also used the symmetry $z \to -z$ which yields

$$\begin{aligned} I = \int_{-\infty}^{\infty} dz \int_{-\pi}^{\pi} d\theta \int_{r_1}^{r_2} ds \frac{e^{-2\rho\zeta}}{4\pi^2} \Bigg[&- \left(\frac{9}{\rho^8\zeta^4} + \frac{18}{\rho^7\zeta^3} + \frac{16}{\rho^6\zeta^2} + \frac{8}{\rho^5\zeta} + \frac{3}{\rho^4} + \frac{\zeta}{\rho^8} \right) \\ &+ s^2 \cos^2\theta \left(\frac{72}{\rho^{10}\zeta^4} + \frac{144}{\rho^9\zeta^3} + \frac{132}{\rho^8\zeta^2} + \frac{72}{\rho^7\zeta} + \frac{28}{\rho^6} + \frac{9\zeta}{\rho^5} + \frac{2\zeta^2}{\rho^4} \right) \Bigg] \\ = \int_{0}^{\infty} dz \int_{r_1}^{r_2} ds \frac{e^{-2\rho\zeta}}{2\pi} \Bigg[&- \left(\frac{18}{\rho^8\zeta^4} + \frac{36}{\rho^7\zeta^3} + \frac{32}{\rho^6\zeta^2} + \frac{16}{\rho^5\zeta} + \frac{6}{\rho^4} + \frac{2\zeta}{\rho^8} \right) \\ &+ s^2 \left(\frac{72}{\rho^{10}\zeta^4} + \frac{144}{\rho^9\zeta^3} + \frac{132}{\rho^8\zeta^2} + \frac{72}{\rho^7\zeta} + \frac{28}{\rho^6} + \frac{9\zeta}{\rho^5} + \frac{2\zeta^2}{\rho^4} \right) \Bigg] , \end{aligned} \tag{3.3.13}$$

with r_1 and r_2 being the inner hollow radius and the outer radius of the cylinder. By inserting all results into (2.6.11), and using $\xi^4 = \varepsilon(i\xi)^{-2}c^4\zeta^4$ we obtain

$$\begin{aligned} \partial_r^2 U_{\mathrm{CP}} = &- \mu_0 k_B T {\sum_{j=0}^{\infty}}' \alpha(i\xi_j) \frac{c^2}{\varepsilon^2(i\xi_j)} \frac{3\varepsilon_{\mathrm{gas}}(i\xi_j)\delta\varepsilon(i\xi_j)}{3\varepsilon_{\mathrm{gas}}(i\xi_j) - \delta\varepsilon(i\xi_j)} \\ &\int_{0}^{\infty} dz \int_{r_1}^{r_2} ds \frac{e^{-2\rho\zeta}}{2\pi} \Bigg[- \left(\frac{18}{\rho^8} + \frac{36\zeta}{\rho^7} + \frac{32\zeta^2}{\rho^6} + \frac{16\zeta^3}{\rho^5} + \frac{6\zeta^4}{\rho^4} + \frac{2\zeta^5}{\rho^3} \right) \\ &+ s^2 \left(\frac{72}{\rho^{10}} + \frac{144\zeta}{\rho^9} + \frac{132\zeta^2}{\rho^8} + \frac{72\zeta^3}{\rho^7} + \frac{28\zeta^4}{\rho^6} + \frac{9\zeta^5}{\rho^5} + \frac{2\zeta^6}{\rho^4} \right) \Bigg] . \end{aligned} \tag{3.3.14}$$

This is calculated using numerical integration. The relative percentage frequency change in the r-axis as functions of the pressure of the gases one at a time is shown in figure 3.4. Here we see the gasses all contribute to increasing the frequency. This is because the magnitude of the Casimir–Polder potential becomes smaller when we add more gas, as the gases have a screening effect on the virtual photons[15]. This effect generally seems to be proportional to the dielectric function of the gas. For instance, the largest dielectric function out of all the gases at low frequencies is that of H_2S. For all spheres, that has the greatest effect on the frequency change at almost all partial pressures. However, we see that there are other mechanisms at play as well. The PTFE sphere seems to have some kind of mechanism decreasing its frequency at higher pressures. This could be due to nontrivial retardation effects [35].

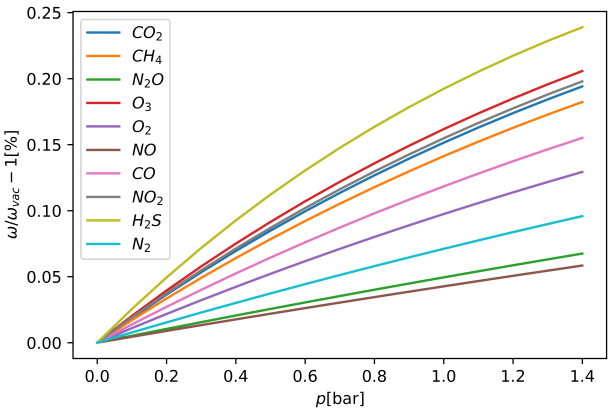

(a) Silica

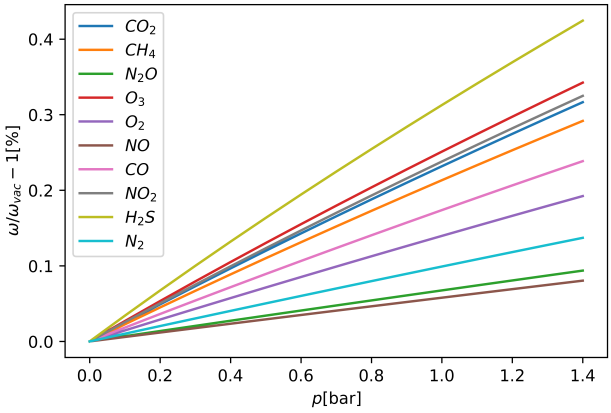

(b) Gallium Arsenide

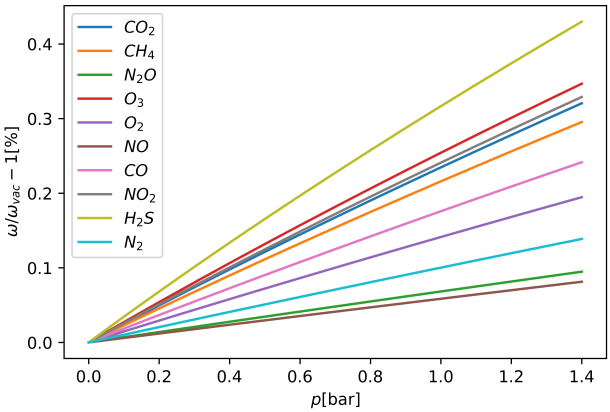

(c) Germanium

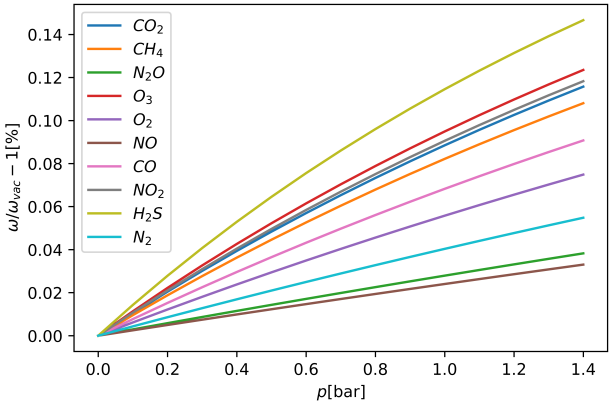

(d) Gold

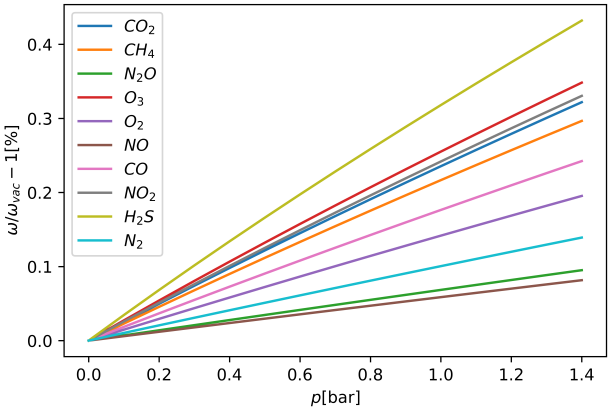

(e) Iridium

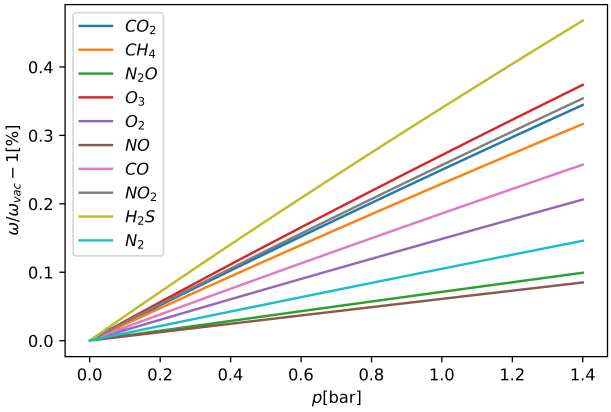

(f) Mica

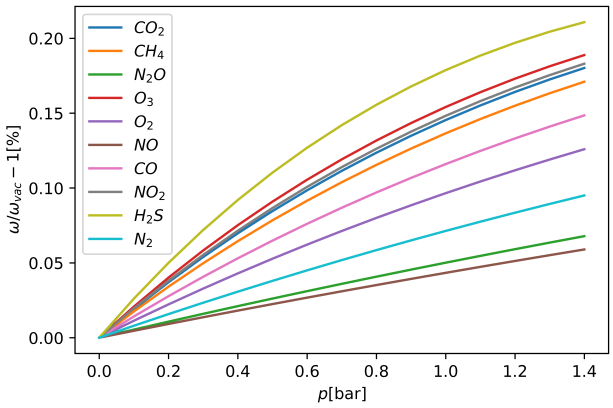

(g) Sodium Chloride

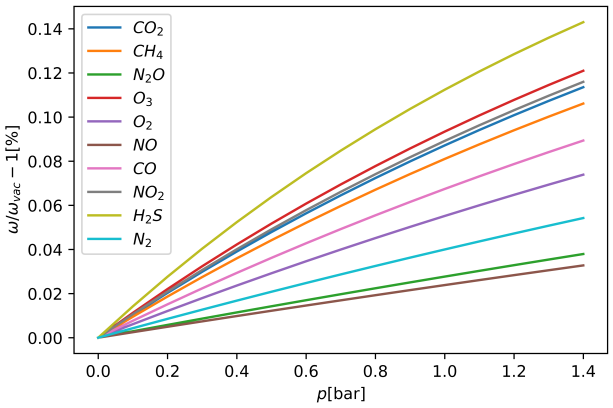

(h) Polystyrene

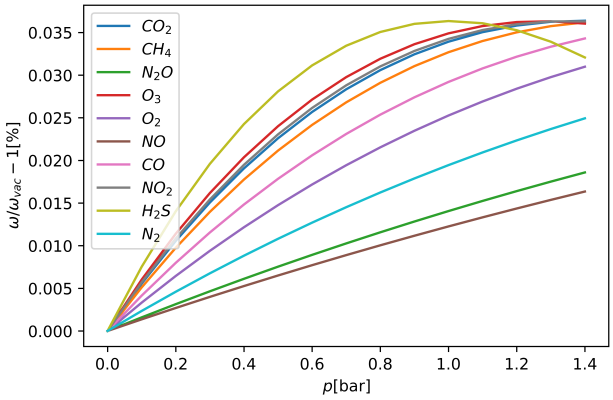

(i) PTFE

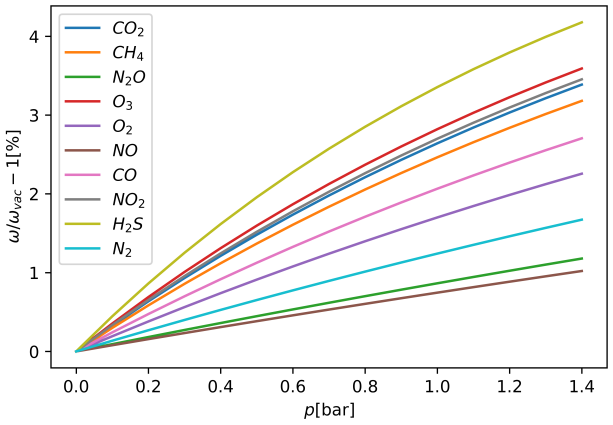

(j) Rutile

Figure 3.4: Plots of relative frequency percentage change $\omega/\omega_{vac} - 1$ as a function of pressure p[bar] for the spheres. Each plot (a)-(f) represents the percentage frequency change of one sphere as we increase the pressure of each gas from 0bar to 1.4bar. The materials for the spheres is (a)Silica, (b)Gallium Arsenide, (c)Germanium, (d)Gold, (e)Iridium, (f)Mica, (g)Sodium Chloride, (h)Polystyrene, (i)PTFE and (j)Rutile. The gases considered are CO_2(blue), CH_4(orange), N_2O(Green), O_3(red), O_2(purple), NO(brown), CO(pink), NO_2(gray), H_2S(olive) and N_2(cyan).

We now generate a large number of gas mixtures by choosing 9 random numbers, a_i between 0 and 1. The gas concentrations are then chosen to be the smallest of the nine numbers minus 0, $a_1 - 0$, the amount of the second gas is chosen to be the second smallest number minus the smallest, $a_2 - a_1$, and so on, $a_i - a_{i-1}$, until the last one being $1 - a_9$. Then ω_z and ω_r are calculated for each of the spheres. The final data set has 39006 different gas mixtures in it.

Chapter 4

Machine Learning

The following chapter explains the machine learning techniques that will be used to attempt to reverse the relationship between different gas concentrations, and the trapping frequencies of the spheres. First, an explanation of neural networks will be given, then a discussion on the specific models used by us and the process by which we decided upon the final one. Some information on how the values of the trapping frequencies are changed before they are fed into the network to make training easier is also given. Then finally, the results of the training will be presented.

4.1 Neural Networks

By machine learning techniques we refer to programs that repeatedly perform tasks to learn how to do them. After each time it has performed the task its performance is measured by a metric, often called a loss. Thereafter the program changes its approach to the task to improve. There are several different methods of improving, such as having multiple slightly different versions of the program and then choosing the best ones, or changing the parameters of your program towards somewhere where the loss is lower. Through repeatedly redoing this process the program gains experience with the task and is often capable of performing the same task in cases it has not seen before.

One example of such an algorithm is a neural network. The dense neural network we use, works by taking a vector of trapping frequencies $[\omega_{r1}, ..., \omega_{r10}, \omega_{z1}, ..., \omega_{z10}]$. More generally any N-vector, $\boldsymbol{x}^{in}$ can be used. This vector is then fed to the first neural network layer, where it is multiplied with a kernel, essentially a $N \times M$-matrix, $\mathbf{A}$. In addition, we add a

bias, $\boldsymbol{b}$. Thus the output of the λ-th layer outputs a M-vector

$$x_i^{(\lambda)} = \sum_j A_{ij}^{(\lambda)} x_j^{(\lambda-1)} + b_i \,, \tag{4.1.1}$$

Equation (4.1.1) is the general form of the λ-th layer in a dense neural network based on the output of the previous layer $\boldsymbol{x}^{(\lambda-1)}$. The output vector is a M-vector. The network is made up of several such hidden layers, possibly all of different sizes, each having as its input the output of the previous layer. The last layer outputs a vector representing the output we want it to reproduce. Such neural networks are often illustrated as a graph with nodes representing the elements of the vectors and lines connecting them representing the weights of the different kernels, like in figure 4.1.

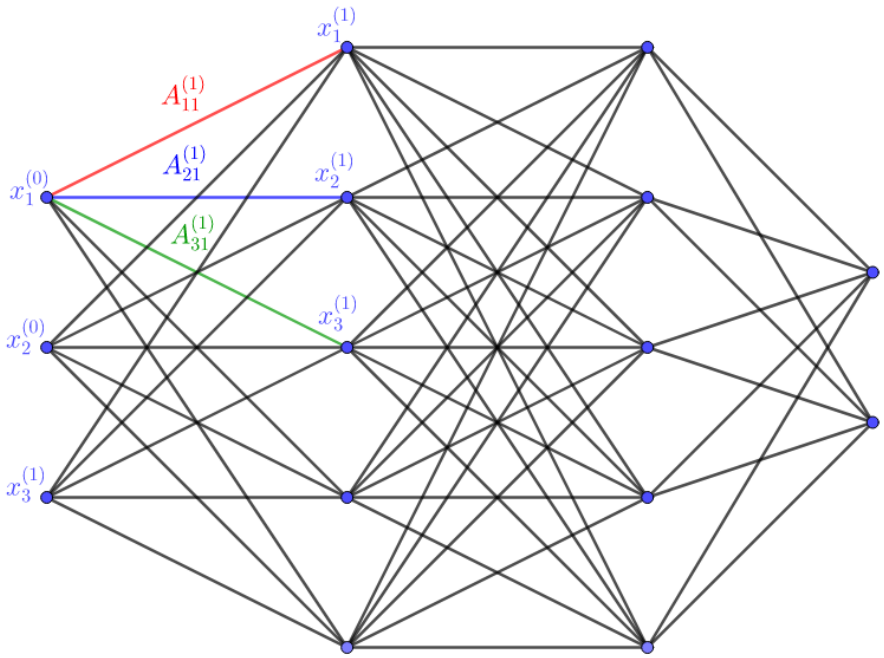

Figure 4.1: Illustration of a dense neural network with some nodes and weights labeled.

The learning part of the algorithm is done by tuning the weights and biases until the output matches the true values we are trying to obtain as close as possible. To do so, we need a measure of how closely our network's guess is to the true values and an algorithm that tunes the weights and biases in such a way that the output becomes closer to the desired values.

Depending on the task, one may use one of many different measurements of performance, known as loss functions, and the value of the loss function is known as the loss of the model.

We choose to use the mean square error loss. When training, we will give the program a batch of cases for it to find the partial pressures of the gases. The mean square error is then the mean of the differences between the true values, $\boldsymbol{t}$, and the output values, $\boldsymbol{x}^{out}$,

$$E = \sum_{n \in N} \frac{(\boldsymbol{x}_n^{out} - \boldsymbol{t}_n)^2}{N} \,. \tag{4.1.2}$$

The next step is to tune the weights of the kernel. There exist many methods for it. Here, we first explain a very simple method called stochastic gradient descent with back-propagation. Initially, the weights are set to be random numbers between some small random numbers, the default values in Keras, a Python library made for machine learning, are -0.05 and 0.05 for the weight and 0 for the biases [36].

For a single gas mixture, we can look at the single case error function E_n as a function of all the weights $\mathbf{A}_{ij}^{(l)}$ in the kernels

$$E_n(A_{11}^{(1)}, A_{12}^{(1)}, ..., A_{11}^{(2)}, ...) = (\boldsymbol{x}_n^{out} - \boldsymbol{t}_n)^2 \,. \tag{4.1.3}$$

As we would like to move towards the smallest possible error, we change $A_{ij}^{(l)}$ by some learning rate η times the derivative of E_n with respect to $A_{ij}^{(l)}$ [16, p.101]

$$\Delta A_{ij}^{(l)} = -\eta \frac{\partial E_n}{\partial A_{ij}^{(l)}} \,. \tag{4.1.4}$$

$x_j^{(l)} = \sum_i A_{ij}^{(l)} x_i^{(l-1)}$ is the weighted sum of inputs to node j, with $\boldsymbol{x}^{(l-1)}$ being the input to layer l. We can imagine the error function E_n as a complicated multi dimensional surface. Moving towards the negative gradient is then the same as moving towards a local minima of the surface. Larger learning rates will allow us to skip over small shallow dips in the surface constituting local minima, however it may skip over deep holes as well. Small learning rates more easily settle in local minima, but might miss better local minima in other places. Thus, choosing the right learning rate for ones problem can be somewhat challenging.

Changing $A_{ij}^{(l)}$ has an effect on the output on the rest of the network through $x_j^{(l)}$, thus [16, p.102]

$$\frac{\partial E_n}{\partial A_{ij}^{(l)}} = \frac{\partial E_n}{\partial x_j^{(l)}} \frac{\partial x_j^{(l)}}{\partial A_{ij}^{(l)}} = \frac{\partial E_n}{\partial x_j^{(l)}} x_i \,. \tag{4.1.5}$$

One now only need expressions for $\frac{\partial E_n}{\partial x_j^{(l)}}$. For the output layer one has that

$$\frac{\partial E_n}{\partial x_j^{out}} = 2(x_j^{out} - t_{n,j})\,. \tag{4.1.6}$$

Thus the stochastic gradient decent rule (4.1.4) becomes

$$\Delta A_{ij}^{out} = 2\eta(x_j^{out} - t_{n,j})x_i^{(out-1)}\,. \tag{4.1.7}$$

For the hidden layer directly before the output layer one has to consider all the downstream consequences of the change as well in a network where the output layer is the L-th layer, using the chain rule one obtains [16, p.103]

$$\frac{\partial E_n}{\partial x_j^{(L-1)}} = \sum_k \frac{\partial E_n}{\partial x_k^{(L)}} \frac{\partial x_k^{(L)}}{\partial x_j^{(L-1)}}\,, \tag{4.1.8}$$

by setting $\frac{\partial E_n}{\partial x_k} = -\delta_k$ yields

$$= \sum_k -\delta_k \frac{\partial x_k^{(L)}}{\partial x_j^{(L-1)}} = \sum_k -\delta_k A_{kj}^{(L-1)}\,, \tag{4.1.9}$$

and the stochastic gradient decent rule (4.1.4) becomes

$$\Delta A_{ij}^{(L-1)} = \sum_k \eta\delta_k A_{kj}^{(L)} x_i^{(L-2)}\,. \tag{4.1.10}$$

For even more hidden layers, such as $L-2$, one has to recursively apply the chain rule, and sum over the contribution from all downstream weights in the next hidden layer, and the next, and so on until you reach the output [37, p.211]. This method is called back-propagation. The example laid out above, is a very specific example and there are other methods of tuning the weights and biases however it illustrates the basic ideas.

We used Keras to generate our neural networks. This is a Python library that automates most of the process of creating a neural network and training it. It has built-in optimizer algorithms such as stochastic gradient descent, commonly abbreviated as SGD, RMSprop, and Adam [36]. These works differently from SGD by, for example, averaging the gradient over a batch of cases, adding momenta, or changing learning rates in the algorithm.

In our case we have been using the RMSprop optimizer. RMSprop works by setting a

parameter, $r_{ij}^{(\lambda)} = 0$ for each $A_{ij}^{(\lambda)}$. Then one repeatedly does the following: Calculate the gradient, $\frac{\partial E}{\partial A_{ij}^{(\lambda)}}$ the same way as before for a small batch of training data. Then, update the parameter $r_{ij}^{(\lambda)}$ such that

$$(r_{ij}^{(\lambda)})_{\text{new}} = \rho(r_{ij}^{(\lambda)})_{\text{old}} + (1-\rho)\left(\frac{\partial E}{\partial A_{ij}^{(\lambda)}}\right)^2 , \tag{4.1.11}$$

with ρ being a decay rate that is 0.9 by default. The weight $A_{ij}^{(\lambda)}$ is then updated according to the rule

$$\Delta A_{ij}^{(\lambda)} = -\frac{\eta}{\sqrt{r}+\varepsilon}\frac{\partial E}{\partial A_{ij}^{(\lambda)}} , \tag{4.1.12}$$

with ε being some small value, in Keras it defaults to 10^{-7}, used to stabilize division by small numbers. Then repeat this until you are satisfied with the training. This results a variable learning rate, and it is often very effective [37, pp.304-305].

4.2 Training Models

For simplicity of training, we will focus on training a network to give us the partial pressure of CO_2 in the gas mixtures we have generated. Here we will present some of the network models we have tried using for training and discuss their performance. We also discuss modifications made to the data to more efficiently train the network and the motivation for these.

Focusing only on CO_2, our true values will be a single number corresponding to the partial pressure of CO_2. Thus, the network should have its output be a single number as well. For the input, we have the trapping frequencies of the spheres in the cylinder. As we use natural units in our code, the trapping frequency oscillations are quite small numbers on the order 10^{-9}, whilst in SI-units they are on the order 10^6. To deal with this we calculate the vacuum trapping frequency and divide the trapping frequencies of our data set by this number, then we subtract one, leaving us with the relative frequency shift due to the presence of the gases. This was motivated by ensuring the data has as much relevant and as little irrelevant information as possible. In that way, the neural networks do not have to spend time learning to separate out vacuum contributions.

The neural networks are trained as new training data was being generated, therefore the size of the data sets in each of the following networks are gradually increasing. We illustrate

the performance of each network with a scatter plot of the predicted values of the validation set against the true values of the CO_2 partial pressure.

All our networks used RMSprop as the optimizer. An initial learning rate of 0.0001 is used. We then train the network for 50 epochs with batch sizes of 1000. This is then repeated 4 more times, for a total of 5 times. The learning rate is then lowered by a factor of 10 and the training is once again repeated 5 more times. This process of lowering the training rate by a factor of 10 and then doing 5 sets of 50 epochs is repeated twice more until the network has been trained with a learning rate of 10^{-7}.

4.2.1 First Model

For the first model, we tried with 3 hidden layers and one dropout layer. The input was a 2×10 tensor, consisting of the 10 z-axis trapping frequencies and the 10 r-axis frequencies. The input layer is then flattened to a flat 1-tensor with 20 entries. This is then fed through a dense neural network layer with 5000 nodes, then it is fed through a dropout layer. This layer randomly chooses connections between nodes to be inactivated halving the number of parameters between the layers. The purpose of this is to increase the training speed by lowering the number of trainable parameters. After the dropout layer, there are two densely connected layers with 10000 nodes in each before the output layer with 1 node. This node has a sigmoid activation, that is it takes its input and puts it in a sigmoid function

$$s(x) = \frac{1}{1 - e^{-x}}\,. \tag{4.2.1}$$

This is done to ensure that our guess stays between 0 and 1, which are the possible values of our training and validation set. Validation data are cases that the network is not trained on. The point of the validation set is to give the network cases it has not seen. In this way, we can confirm that the network has learned how to measure the partial pressure, and not just memorized the training data. The phenomena of the network learning the data set instead of the rules of the data set is known as overfitting and can be seen when the validation loss becomes bigger than the training loss.

The neural networks structure is summarized in table 4.1. The performance of this network is summarized in figure 4.2. Here, we have first plotted the neural network's guesses for the validation data after having only trained on a small training data set. We have also plotted the results with a bigger training data set to show how increasing the amount

Layer (type)	Output Shape	Parameters
InputLayer	[(None, 2, 10, 1)]	0
Flatten	(None, 20)	0
Dense	(None, 5 000)	105 000
Dropout	(None, 5 000)	0
Dense	(None, 10 000)	50 010 000
Dense	(None, 10 000)	100 010 000
Dense	(None, 1)	10 001
Total parameters: 150 135 001		
Trainable parameters: 150 135 001		
Non-trainable parameters: 0		

Table 4.1: Overview of the first model training was done on. Showing the types of layers used, the shape of the layers and the number of trainable parameters in each layer.

of training data can improve the final performance. A perfect network would be able to perfectly place all points on the line $y = x$ in these plots. Currently, we see a line that starts above this line, then curves below it, and then above again. In the second example, it starts curving back towards the line again in the high partial pressure cases, making a sort of s-shape. This first model has over 150 million trainable parameters. This large number makes training quite slow, as calculating the derivatives of the parameters takes a long time. We will make the network faster by having a smaller shape for each layer in the network. To still be able to find complicated patterns, we will also add more layers.

4.2.2 Second Model

The second model, we made, is summed up in table 4.2. It only has a little over 6 million trainable parameters, and training is therefore much quicker. In addition to having more hidden layers, this network also has the benefit of having a bigger data set to train on. Its performance is plotted in figure 4.3. There, we see the guesses staying closer to the line than in the first model's case. However, it still wiggles up and down except for at high partial pressures. There, it guesses much lower values for the partial pressure. At this point, we recognized the shape of the guess function as being caused by the sigmoid activation (4.2.1). To minimize the overall loss, the less common cases where the partial pressure is large have the bulk of the sigmoid activation problem.

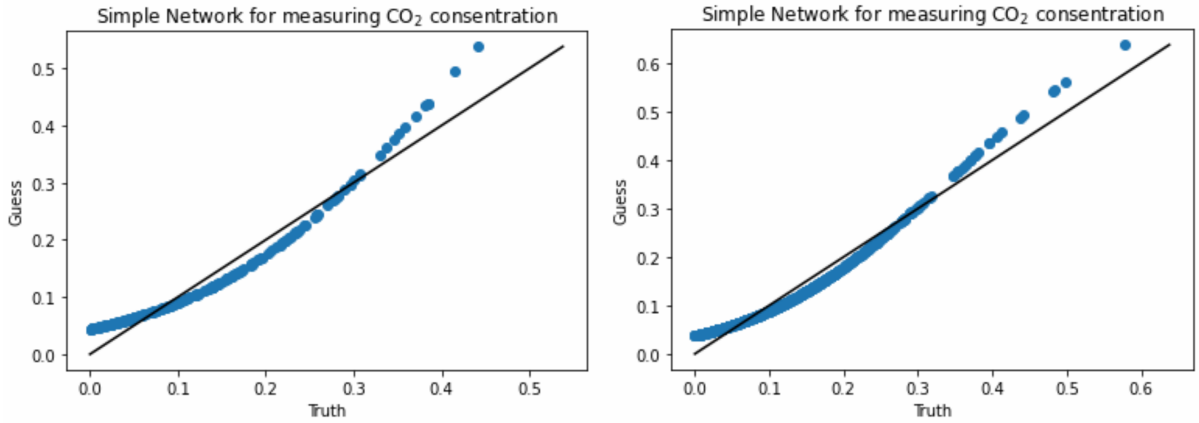

(a) (b)

Figure 4.2: The first networks guess value[atm] plotted against the true value[atm] of CO_2 partial pressure . (a) illustrates the result with a small sample of training data. (b) illustrates the result with a larger sample of training data. The black line illustrates where perfect guesses would be.

Layer (type)	Output Shape	Parameters
InputLayer	[(None, 2, 10, 1)]	0
Flatten	(None, 20)	0
Dense	(None, 1 000)	21 000
Dense	(None, 1 000)	1 001 000
Dense	(None, 1 000)	1 001 000
Dense	(None, 1 000)	1 001 000
Dense	(None, 1 000)	1 001 000
Dense	(None, 1 000)	1 001 000
Dense	(None, 1 000)	1 001 000
Dense	(None, 100)	100 100
Dense	(None, 100)	10 100
Dense	(None, 100)	10 100
Dense	(None, 1)	101
Total parameters: 6 147 401		
Trainable parameters: 6 147 401		
Non-trainable parameters: 0		

Table 4.2: Overview of the second model training was done on. Showing the types of layers used, the shape of the layers and the number of trainable parameters in each layer.

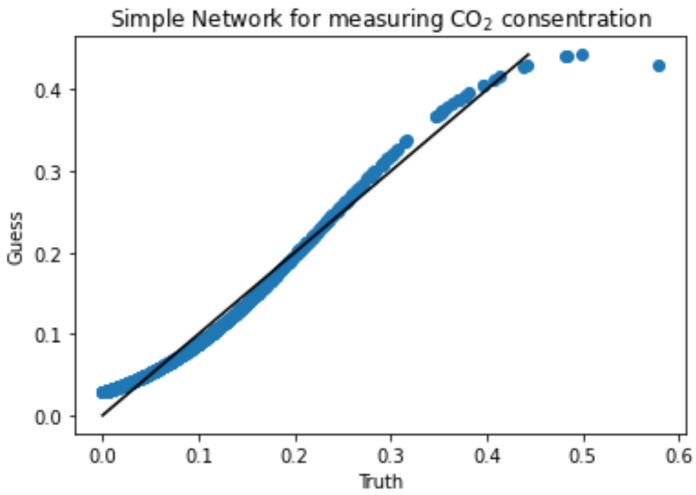

Figure 4.3: The second networks guess value[atm] plotted against the true value[atm] of CO_2 partial pressure. The black line illustrates where perfect guesses would be.

4.2.3 Third Model

Due to the large discrepancy at large partial pressures, we change the activation of our model to a ReLu activation, that is $x^{out} = 0$ if $x^{out} < 0$, and $x^{out} = x^{out}$ otherwise [36]. We also once again made more data to train on and made a new neural network structure. Once again we made it deeper, by adding more layers, and we made the layers smaller. The third model is summed up in table 4.3, and the performance in figure 4.4. Here, we see that the s-shape caused by the sigmoid activation is gone. And it now seems to follow a slightly wobbly line, with a slightly lower gradient than the actual line. The next section discusses the changes done to this model to reach our final model.

Layer (type)	Output Shape	Parameters
InputLayer	[(None, 2, 10, 1)]	0
Flatten	(None, 20)	0
Dense	(None, 288)	6 048
Dense	(None, 288)	83 232
Dense	(None, 288)	83 232
Dense	(None, 288)	83 232
Dense	(None, 288)	83 232
Dense	(None, 288)	83 232
Dense	(None, 288)	83 232
Dense	(None, 288)	83 232
Dense	(None, 288)	83 232
Dense	(None, 288)	83 232
Dense	(None, 288)	83 232
Dense	(None, 288)	83 232
Dense	(None, 288)	83 232
Dense	(None, 1)	289
Total parameters: 921 889		
Trainable parameters: 921 889		
Non-trainable parameters: 0		

Table 4.3: Overview of the final model training was done on. Showing the types of layers used, the shape of the layers and the number of trainable parameters in each layer.

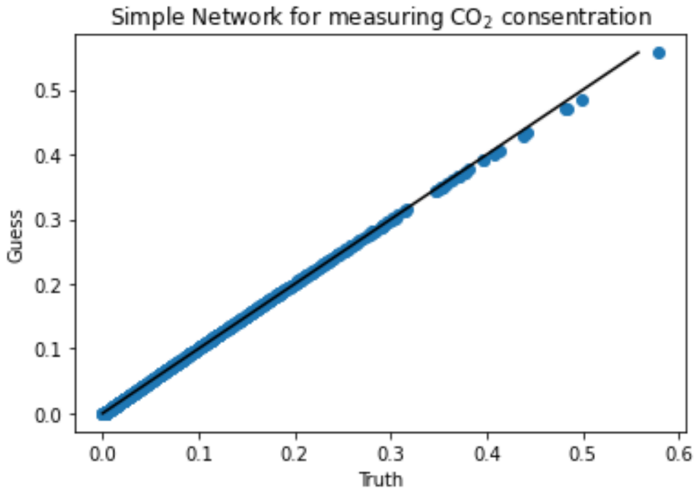

Figure 4.4: The third models guess values[atm] plotted against the true value[atm] of CO_2 partial pressure. The black line illustrates where perfect guesses would be.

Chapter 5

Results

This chapter presents our final neural network model and its performance. We also discuss the applicability of our results and their meaning.

The final model is trained on the first 37006 gas mixtures in the data set. The remaining 2000 points are used as a validation set. It has the same structure as the third model, see figure 4.4, but it has ReLu activation on all layers. Its performance is shown in figure 5.1. We see that it almost perfectly follows the black line except for what seems to be a very slightly lower gradient. More data might help fix this as a few cases with high partial pressure makes it harder for the network to become good at predicting these cases.

The final model has a validation loss of 4.27×10^{-9} atm^2, the square root of which is 6.53×10^{-5} atm. This is an approximation of the sensors uncertainty. This corresponds to an uncertainty of ± 6.62 Pa. The most common cases are cases where the partial pressure of CO_2 is around 0.1 atm. If we limit our validation test to cases with CO_2 concentrations between 0.08 atm and 0.12 atm, of which there are 296, the mean square error is 3.55×10^{-10} atm^2 and the root of this is 1.88×10^{-5} atm, corresponding to an uncertainty of ± 1.91 Pa. At 0.1 atm that is a relative uncertainty of 0.0188%. Further, form 0.1 atm, especially at much lower concentrations the relative uncertainty is higher. If we had trained with mainly lower partial pressure cases or higher partial pressure cases the relative uncertainty in these cases might have been different.

The training loss is 1.00×10^{-9} atm^2, which is about a fourth of the validation loss. This indicates that the neural network is starting to overfit. In figure 5.2, we can see that the validation loss roughly follows the loss up until about epoch 750, where we switch to a learning rate of 10^{-7}. At that point, the validation loss remains somewhat stable at a higher

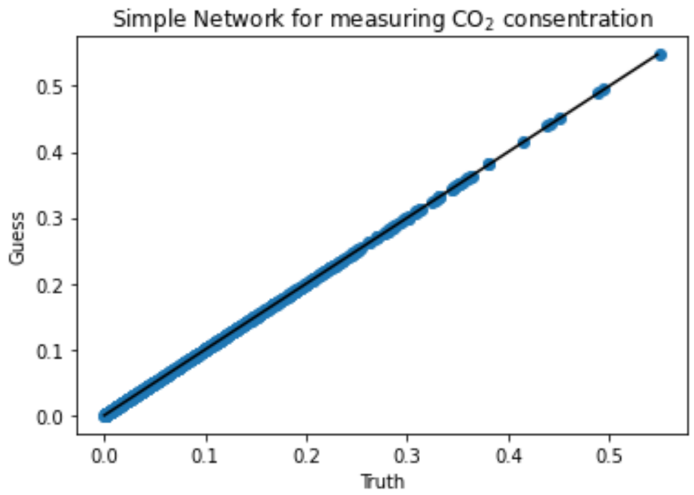

Figure 5.1: The final networks guess values[atm] plotted against the true value[atm] of CO_2 partial pressure. The black line illustrates where perfect guesses would be.

value than the training loss. Therefore, we stop the training at this point, as training beyond this point has no positive effect on the accuracy of the neural network.

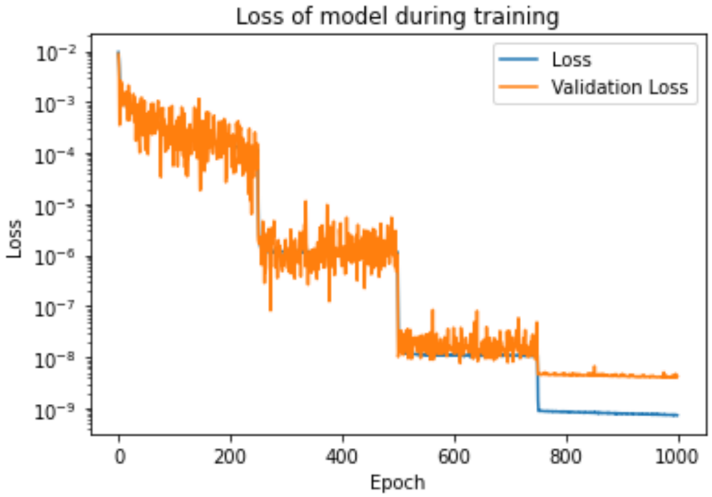

Figure 5.2: Loss and validation loss of the final neural network during training.

During the training, we see the loss suddenly dropping by orders of magnitude several times. This corresponds to when we change the learning rate. The reason we don't choose a low learning rate from the start is due to the network constantly getting stuck in local minima with much higher losses when we do so.

The goal of this thesis was to investigate the possibility of using the quantum vacuum fluctuations of the electromagnetic field to measure the partial pressure of a gas in a gas

mixture. In this section, we will discuss if we can be sure that this is what the network is doing. The gas mixture has 10 constituents. The permittivity at some specific wavelength is therefore defined by 10 different variables. Thus, for any wavelength most values of permittivity could indicate a large number of possible gas mixtures. As the optical potential used only has information about the permittivity of the gas mixtures at one specific wavelength it is not possible to separate the constituents of the gas out from this term alone.

The only other term that affects the trapping frequencies is the double derivative of the Casimir–Polder potential. This depends on the permittivity for a large number of different frequencies and thus can in theory encode different information about the permittivity for each sphere.

This shows that the only way for the network to separate out the partial pressures is if the Casimir–Polder potential of the spheres has encoded parts of the spectra in the trapping frequency. Having consistently separated the partial pressure of CO_2 from a mixture of 10 different gases with a good level of accuracy, we can say, we used quantum vacuum fluctuations to measure the partial pressure of CO_2.

Chapter 6

Conclusion and Outlook

This thesis models a gas detector made of optically trapped spheres in a hollow-core fiber. We have shown how dielectric spheres react to electromagnetic fields, and we have shown how the quantized electromagnetic field leads to forces arising between neutral atoms and their surroundings, specifically through the Casimir–Polder potential.

For a large set of gas mixtures, 39006 mixtures, the trapping potential and the Casimir–Polder potential is approximated using the Born series expansion. From this, the trapping frequencies in two directions are calculated. This data set of trapping frequencies is then used to train an artificial neural network that can distinguish the partial pressure of CO_2 with a mean square error validation loss of 4.27×10^{-9} atm^2, corresponding to an uncertainty of ± 6.62 Pa. Thus, we have shown that quantum vacuum fluctuations might be used to do spectroscopy on gases.

While we have shown that these fluctuations can be used to measure the partial pressure of a gas, more work still needs to be done before such a sensor might be built. First of all, our thesis assumes a lot of ideal conditions, such as the atom always being in its ground state and that there is no significant effect from resonance frequencies. These assumptions would not hold in a real system as thermal fluctuations and interactions with the laser would excite the electrons in the spheres atoms.

Our description of the laser field is very simplistic and does not accurately describe what a real field in a hollow-core fiber would look like. A proper description of this as well as a description of how the atoms would react to it is also required if one wishes to perform experiments with a system similar to our model.

Doing training on data with more cases with much higher or much lower concentrations

will give probably give lower relative uncertainties for these new cases in. Doing training on low concentration cases and no CO_2 cases should also be done in order to test the sensitivity, being the probability of true positive measurements, and specificity, being the probability of true negative measurements, of such sensors.

It would be interesting to try to train our model on more gases. It could also be an idea to try to make a model capable of separating out multiple gases at once. This might require more spheres or some other modification to the detector model.

The gases used in this thesis have small molecules, and therefore most of their resonances are in the visible region. If we wish to look for the presence of larger molecules, where the bonds between the atoms create resonances in the infrared region we need to adapt the spheres to be sensitive in this spectral range. The contribution to the Casimir–Polder potential is bigger from the lower frequencies. With more sensitive sensors it would be interesting to instead try to train a classifier to make a single particle detector. Investigations into such a sensors sensitivity and specificity would then be required.

It would also be interesting to attempt to find a more accurate solution to the Casimir–Polder potential. Analytical solutions for the electromagnetic Green tensor in multilayered cylindrical media do exist [38], and using these instead of the Born series expansion might give different results.

Finally, it would be possible to make a gas sensor via repeated measurements of the trapping frequencies.

Bibliography

[1] Alireza Khalilian, Md. Rajibur Rahaman Khan, and Shin-Won Kang. Highly sensitive and wide-dynamic-range side-polished fiber-optic taste sensor. *Sensors and Actuators B: Chemical*, 249:700–707, 2017.

[2] T Vo-Dinh and B Cullum. Biosensors and biochips: advances in biological and medical diagnostics. *Fresenius' Journal of Analytical Chemistry*, 366(6):540–551, 2000.

[3] Abdulkadir Yurt, George G Daaboul, John H Connor, Bennett B Goldberg, and M Selim Ünlü. Single nanoparticle detectors for biological applications. *Nanoscale*, 4(3):715–726, feb 2012.

[4] A. Juzgado, A. Soldà, A. Ostric, A. Criado, G. Valenti, S. Rapino, G. Conti, G. Fracasso, F. Paolucci, and M. Prato. Highly sensitive electrochemiluminescence detection of a prostate cancer biomarker. *J. Mater. Chem. B*, 5:6681–6687, 2017.

[5] Adriano Cavalcanti, Bijan Shirinzadeh, Mingjun Zhang, and Luiz C. Kretly. Nanorobot hardware architecture for medical defense. *Sensors*, 8(5):2932–2958, 2008.

[6] S Y Oh, B Cornell, D Smith, G Higgins, C J Burrell, and T W Kok. Rapid detection of influenza A virus in clinical samples using an ion channel switch biosensor. *Biosensors and Bioelectronics*, 23(7):1161–1165, 2008.

[7] Stefan Scheel and Stefan Y Buhmann. Macroscopic Quantum Electrodynamics - Concepts and Applications. *acta physica slovaca*, 2008.

[8] H. B. G. Casimir. On the attraction between two perfectly conducting plates. *Proc. Akad. Wet. Amsterdam*, 51:793–795, 1948.

[9] F. London. Zur Theorie und Systematik der Molekularkräfte. *Zeitschrift für Physik*, 63:245–279, 1930.

[10] H. B. G. Casimir and D. Polder. The Influence of Retardation on the London-van der Waals Forces. *Phys. Rev.*, 73:360–372, Feb 1948.

[11] Johannes Fiedler, Drew F. Parsons, Friedrich Anton Burger, Priyadarshini Thiyam, Michael Walter, I. Brevik, Clas Persson, Stefan Yoshi Buhmann, and Mathias Boström. Impact of effective polarisability models on the near-field interaction of dissolved greenhouse gases at ice and air interfaces. *Phys. Chem. Chem. Phys.*, 21:21296–21304, 2019.

[12] Carolyn D. Ruppel and John D. Kessler. The interaction of climate change and methane hydrates. *Reviews of Geophysics*, 55(1):126–168, 2017.

[13] Mathias Boström, Victoria Esteso, Johannes Fiedler, Iver Brevik, Stefan Yoshi Buhmann, Clas Persson, Sol Carretero-Palacios, Drew F. Parsons, and Robert W. Corkery. Self-preserving ice layers on CO2 clathrate particles: implications for enceladus, pluto and similar ocean worlds. *Astronomy and Astrophysics*, 650:A54, 2021.

[14] Joshua L. Hemmerich, Robert Bennett, Thomas Reisinger, Stefan Nimmrichter, Johannes Fiedler, Horst Hahn, Herbert Gleiter, and Stefan Yoshi Buhmann. Impact of Casimir–Polder interaction on Poisson-spot diffraction at a dielectric sphere. *Phys. Rev. A*, 94:023621, Aug 2016.

[15] Johannes Fiedler, Michael Walter, and Stefan Yoshi Buhmann. Effective screening of medium-assisted van der Waals interactions between embedded particles. *The Journal of Chemical Physics*, 154(10):104102, 2021.

[16] Tom M. Mitchell. *Machine Learning*. McGraw-Hill, New York, 1997.

[17] Gerald B. Folland. *Fourier Analysis and Its Applications*. Pure and Applied Undergraduate Texts. American Mathematical Society, 4th edition, 2009.

[18] Ben Yu-Kuang Hu. Kramers-Kronig in two lines. *American Journal of Physics*, 57(9):821–821, September 1989.

[19] Arfken G. *Mathematical methods for physicists*. Academic Press, Inc, 3 edition, 1985.

[20] R. de L. Kronig. On the theory of dispersion of x-rays. *J. Opt. Soc. Am.*, 12(6):547–557, Jun 1926.

[21] H. A. Kramers. La diffusion de la lumière par les atomes. *Atti del Congresso Internationale dei Fisici*, pages 545–557, 1927.

[22] S. Buhmann. *Lecture notes on Theoretical quantum optics*, 2017.

[23] F Mandl and G Shaw. *Quantum field theory*. Wiley, 2nd edition, 2010.

[24] C. J. Böttcher (Auth.). *Theory of Electric Polarization. Dielectrics in Static Fields*. Amsterdam Elsevier, 2nd ed. completely rev edition, 1973.

[25] John David Jackson. *Classical electrodynamics*. Wiley, New York, 3rd ed. edition, 1999.

[26] David J Griffiths. *Introduction to Electrodynamics*. Cambridge University Press, Cambridge, 4th ed. edition, 2017.

[27] S. Buhmann. *Dispersion Forces II: Many-Body Effects, Excited Atoms, Finite Temperature and Quantum Friction*. Springer Tracts in Modern Physics. Springer Berlin Heidelberg, 2013.

[28] David J Griffiths. *Introduction to Quantum Mechanics*. Cambridge University Press, 3rd edition, 2017.

[29] Johannes Fiedler, Priyadarshini Thiyam, Anurag Kurumbail, Friedrich A. Burger, Michael Walter, Clas Persson, Iver Brevik, Drew F. Parsons, Mathias Boström, and Stefan Y. Buhmann. Effective Polarizability Models. *The Journal of Physical Chemistry A*, 121(51):9742–9751, Dec 2017.

[30] D. E. Aspnes. Local-field effects and effective-medium theory: A microscopic perspective. *American Journal of Physics*, 50(8):704–709, 1982.

[31] Friedrich Anton Burger, Robert William Corkery, Stefan Yoshi Buhmann, and Johannes Fiedler. Comparison of Theory and Experiments on van der Waals Forces in Media—A Survey. *The Journal of Physical Chemistry C*, 124(44):24179–24186, 2020.

[32] P. J. van Zwol and G. Palasantzas. Repulsive Casimir forces between solid materials with high-refractive-index intervening liquids. *Phys. Rev. A*, 81:062502, Jun 2010.

[33] Edward Palik. *Handbook of optical constants of solids*. Academic Press, 1998.

[34] G. Epple, K. S. Kleinbach, T. G. Euser, N. Y. Joly, T. Pfau, P. St. J. Russell, and R. Löw. Rydberg atoms in hollow-core photonic crystal fibres. *Nature Communications*, 5(1), Jun 2014.

[35] Johannes Fiedler, Kristian Berland, Fabian Spallek, Iver Brevik, Clas Persson, Stefan Yoshi Buhmann, and Mathias Boström. Nontrivial retardation effects in dispersion forces: From anomalous distance dependence to novel traps. *Phys. Rev. B*, 101:235424, Jun 2020.

[36] F. Chollet et al. Keras ,https://github.com/keras-team/keras, 2022.

[37] Ian Goodfellow, Yoshua Bengio, and Aaron Courville. *Deep Learning*. MIT Press, 2016. `http://www.deeplearningbook.org`.

[38] L.-W. Li, M.-S. Leong, T.-S. Yeo, and P.-S. Kooi. Electromagnetic Dyadic Green's Functions in Spectral Domain for Multilayered Cylinders. *Journal of Electromagnetic Waves and Applications*, 14(7):961–985, 2000.